

Probabilistic calibration of crystal plasticity material models with synthetic global and local data

Joshua D. Pribe^{a,*}, Patrick E. Leser^b, Saikumar R. Yeratapally^c, George Weber^b

^a*Analytical Mechanics Associates, Hampton, VA 23666*

^b*NASA Langley Research Center, Hampton, VA 23681*

^c*Science and Technology Corporation, Hampton, VA 23666*

Abstract

Crystal plasticity models connect macroscopic deformation with the physics of microscale slip in polycrystalline materials. These models can be calibrated using global stress-strain curves, but the resulting parametrization is often not unique: multiple parametrizations can predict the same global behavior but different local, grain-scale behavior. Using local data for calibration can mitigate uniqueness issues, but expensive specialized experiments like high-energy X-ray diffraction (HEDM) are typically required to gather the data. The computational expense of full-field simulations also often prevents uncertainty quantification with sampling-based calibration algorithms like Markov chain Monte Carlo. This study presents a two-stage calibration procedure that combines global and local data and balances the efficiency of a surrogate model with the accuracy of full-field crystal plasticity simulations. The procedure quantifies uncertainty using Bayesian inference with an efficient, parallelized sequential Monte Carlo algorithm. Calibrations are completed using synthetic data with a microstructure representative of Inconel 718 to assess uncertainty and accuracy of the parameters relative to a known ground truth. Global data comes from the uniaxial stress-strain curve, while local data comes from grain-average stresses, reflecting typical outputs of HEDM experiments. Additional calibrations with limited and noisy local data demonstrate robustness of the procedure and identify the most important features of the data. Overall, the results demonstrate the computational efficiency of the two-stage procedure and the value of local data for reducing parameter uncertainty. In addition, joint distributions of the calibrated parameters highlight key considerations in choosing constitutive models and calibration data, including challenges resulting from correlated parameters.

Keywords: crystal plasticity; Inconel 718; sequential Monte Carlo; calibration; uncertainty quantification

1. Introduction

Crystal plasticity (CP) models have become powerful tools for predicting deformation and failure in polycrystalline metals. Initial models focused primarily on explaining macroscale behavior, including stress-

*Corresponding author. E-mail: joshua.pribe@nasa.gov

strain curves and texture development under large deformations (Taylor, 1934; Bishop and Hill, 1951). Over time, increasingly detailed constitutive models have been developed and used with full-field solvers to predict local behavior like mesoscale cyclic deformation and fatigue crack initiation in engineering alloys (Peirce et al., 1983; Anand and Kothari, 1996; Roters et al., 2010; Lebensohn and Rollett, 2020). However, especially for complex phenomenological models with many parameters, independently calibrating all model parameters with limited experimental measurements can be extremely challenging (Hochhalter et al., 2020).

Traditional calibration approaches for CP models rely on macroscale or global measurements, such as uniaxial stress-strain curves (Rovinelli et al., 2017; Bandyopadhyay et al., 2019; Herrera-Solaz et al., 2014). However, many studies have demonstrated that multiple CP parameter sets may be consistent with the global stress-strain curve, yet predict widely varying responses for single crystals (Sangid et al., 2014; Dindarlou and Castelluccio, 2022; Shimanek et al., 2025). In other words, calibrating a model using the global stress-strain curve alone results in a lack of unique and identifiable parameters. The non-unique parametrization in turn can cause the model to be unreliable for predicting local quantities of interest, such as intragranular stress concentrations and fatigue indicator parameters (Ashraf and Castelluccio, 2023). Therefore, to predict extrema of local fields, it is crucial to incorporate data at multiple scales, including the scale of individual grains, into calibration and validation processes (Shade et al., 2019; Pokharel et al., 2014; Sangid, 2020).

High-fidelity measurement techniques have recently begun to provide access to local measurement data. For example, high-energy X-ray diffraction microscopy (HEDM) measurements can be used to estimate grain-average elastic strains, and thereby infer stresses, in three dimensions Shade et al. (2019). High-energy synchrotrons enable HEDM data to be collected through the thickness of millimeter-scale specimens during in-situ loading experiments Obstalecki et al. (2014). HEDM has been used to perform detailed validation studies of CP predictions at the scale of individual grains within a polycrystal (Menasche et al., 2021, 2023; Mackey et al., 2023; Prithivirajan et al., 2021; Yeratapally et al., 2021). High-resolution electron backscatter diffraction (HR-EBSD) provides similar data, but only on the surface of a specimen. During an in-situ loading experiment in a scanning electron microscope (SEM), HR-EBSD combined with digital image correlation (DIC) can estimate local elastic strains, plastic strains, and dislocation densities, enabling validation of plastic slip predictions (Stinville et al., 2022; Zhang et al., 2016). However, local measurements from both HR-EBSD and HEDM are limited due to the time and monetary costs of operating SEMs and especially synchrotrons (Shade et al., 2019; Hochhalter et al., 2020). As a result, it is important to understand how many and what types of measurements to make with these techniques.

Single-crystal measurements are a possible alternative to local data from polycrystalline specimens, but these measurements involve several challenges. Single-crystal stress-strain curves also can be highly sensitive to small alignment errors between the intended crystallographic loading direction and the actual load fixture, resulting in significant uncertainty or errors in calibrated parameters (Shimanek et al., 2024; Dindarlou and Castelluccio, 2024; Shimanek et al., 2025). It is also often challenging and expensive to

produce or extract and mechanically test single crystals for engineering alloys not specifically designed to be used in single-crystal applications, while the single-crystal specimens can have microstructural differences from their polycrystalline counterparts (Lodh et al., 2023; Dindarlou and Castelluccio, 2024). This study therefore focuses on multiscale data from polycrystals.

In addition to limited measurement data, CP calibration studies have encountered significant challenges in the calibration process itself. Perhaps most importantly, computational cost is a major concern for full-field CP computations. Hand-tuning the model parameters is the simplest approach (Cheng et al., 2024; Liu et al., 2020; Park et al., 2019) but becomes more difficult as the number of parameters increases and provides minimal information about parameter accuracy, uncertainty, and proximity to the minimum of some objective function. Deterministic methods like gradient-based optimization are more rigorous than hand-tuning but still typically provide only point estimates of the calibration parameters. Deterministic optimization algorithms also often converge to one of many local minima due to non-uniqueness in the high-dimensional parameter space, complex parameter interactions, limited data, and measurement noise (Hochhalter et al., 2020; Depriester et al., 2023). Probabilistic methods like Bayesian inference instead provide both point estimates and uncertainty quantification (UQ) for the parameters, which can be crucial for predicting reliability (Fernandez-Zelaia et al., 2022; Whelan and McDowell, 2019). However, probabilistic calibrations typically use sampling methods like Markov chain Monte Carlo (MCMC) that can require many thousands of model evaluations, greatly increasing cost over deterministic methods (Hochhalter et al., 2020).

Existing strategies for computationally tractable calibration with a full-field CP model all involve significant trade-offs. First, efficient surrogate models like Gaussian processes have been used in a variety of deterministic and probabilistic calibration schemes in place of full-field CP simulations (Nguyen et al., 2021; Fernandez-Zelaia et al., 2022; Veasna et al., 2023). However, the resulting calibration can be biased due to discrepancies between the surrogate and the CP model, and the prediction error and training costs scale with the dimensionality of the inputs (i.e., calibration parameters) and outputs (i.e., adding local measurement data) (Nguyen et al., 2021; Brynjarsdóttir and O’Hagan, 2014). For calibrations that rely on repeatedly evaluating the full-field CP model, genetic algorithms (Bandyopadhyay et al., 2019; Kapoor et al., 2021; Weber et al., 2022) and Bayesian optimization (Kuhn et al., 2022; Tran and Lim, 2023; Shi-manek et al., 2025) are the most commonly used techniques since they do not require derivatives of the CP model and thereby avoid robustness issues with gradient-based optimization. Both techniques return only point estimates of the calibration parameters, although Bandyopadhyay et al. (2019) did basic UQ using repeated genetic algorithm runs and restrictive assumptions about the normality and independence of the calibrated parameter realizations. More rigorous UQ using MCMC with full-field CP models is generally seen as computationally intractable (Hochhalter et al., 2020; Bandyopadhyay et al., 2019).

Finally, two-stage calibration approaches were used by Depriester et al. (2023) and Nguyen et al. (2021) with the goal of obtaining informative initial guesses or prior distributions that reduce the number of required

evaluations of a full-field CP model. Both used an inexpensive model with global uniaxial data in the first stage and introduced local data from tensile DIC measurements and plate impact data, respectively, in the second stage. Depriester et al. (2023) used a full-field CP model and deterministic optimization in the second stage but still encountered uniqueness issues and extreme computational costs (about 55 days of walltime) despite incorporating information from the inexpensive first stage. Nguyen et al. (2021) trained a Gaussian process surrogate for their CP model in the second stage on a restricted parameter space informed by the first stage output. The surrogate model allowed for UQ through Bayesian inference but is subject to the limitations of surrogate models noted previously, and the authors also commented that hand-tuning some of the parameters was “more straightforward” (Nguyen et al., 2021).

1.1. Contribution of this study

This study addresses two gaps in prior work. First, a two-stage probabilistic calibration procedure is presented that addresses previous computational bottlenecks while mitigating surrogate-induced bias by using the full CP model. The calibration uses Bayesian inference with both global and local data to obtain CP parameter estimates with UQ. The first stage of the calibration uses a neural network surrogate model to infer preliminary posterior distributions for the model parameters based on only the global data. The posteriors then serve as informative prior distributions for the second stage, which uses a full-field CP model with the global and local data to infer the final posterior distributions for the model parameters. The informative priors are intended to reduce the number of required model evaluations. Finally, an efficient, parallelizable sequential Monte Carlo (SMC) algorithm is used to sample from the posterior distributions of the parameters in each stage. The two-stage approach and SMC parallelization mitigate the prohibitive computational costs for doing Bayesian inference with full-field CP models. The overall workflow for the two-stage approach is shown in Fig. 1

Second, while prior work has shown that local data is needed to resolve parameter uniqueness issues, it is necessary to assess how the availability and quality of this data affects the uncertainty in the calibrated parameters. In this study, results from several calibration runs with different model assumptions and data availability are compared, including calibrations with global data only, local data with increased measurement noise, and with and without a surrogate model. Synthetic measurement data is used in all calibrations and generated by a CP simulation with ground-truth parameters based on the nickel-base superalloy Inconel 718 (Stinville et al., 2022; Bandyopadhyay et al., 2019). Objectives include understanding how the local data affects the calibration results, quantifying the robustness of the two-stage approach to limited or noisy local data, and assessing the implications for how constitutive models and calibration experiments should be selected.

The remainder of this study is organized as follows. Section 2 describes the CP formulation, including the spectral solver, constitutive model, microstructure, and boundary conditions. Section 3 describes the

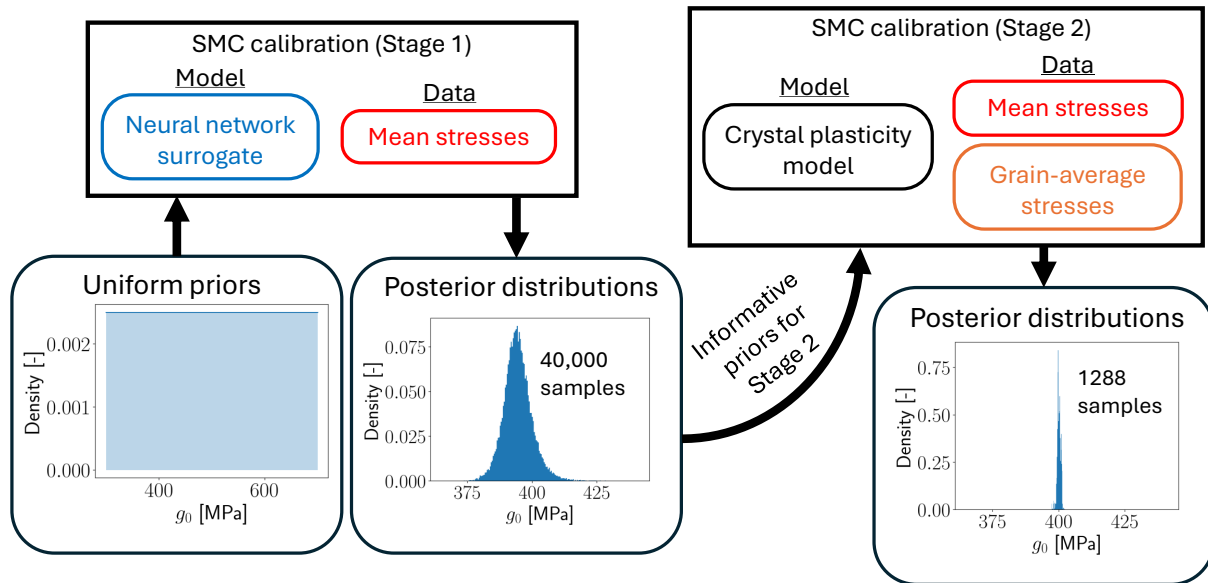


Figure 1: Workflow for the two-stage calibration procedure. Stage 1 uses uniform prior distributions on each parameter, the neural network surrogate model, and the synthetic mean stress data. Stage 2 uses priors based on a kernel density estimate of the material parameter posterior distributions from stage 1, the full CP model, and both the synthetic mean and grain-average stress data.

SMC algorithm, calibration parameters, and synthetic measurement data. Section 4 presents posterior distributions from the proposed two-stage calibration approach, as well as comparisons that address the objectives in the previous paragraph. Section 5 highlights advantages and limitations of the calibration approach based on the numerical results and describes challenges and potential solutions for applying the approach to real measurement data. Finally, Section 6 summarizes key conclusions of this study.

2. Crystal plasticity simulations

The CP simulations in this paper are based on the small-strain Fourier-Galerkin scheme of Zeman et al. (2017); de Geus et al. (2017). The stress and strain are computed on a regular grid of voxels and approximated using trigonometric polynomial shape functions. The Fourier-Galerkin approach does not rely on a reference medium required by other spectral methods (e.g., Moulinec and Suquet (1998)) and instead defines a projection operator that enforces compatibility and equilibrium in Fourier space. Specific components of the projection tensor are used to define the stress and strain boundary conditions (Lucarini and Segurado, 2019). Further details can be found in Appendix A. The model was implemented in version 0.1 of the open-source code Materialite¹ developed at NASA Langley Research Center.

¹Available under the Apache 2.0 license at <https://github.com/nasa/materialite>.

2.1. Constitutive model

The small-strain CP model in this work is based on the standard additive decomposition of the strain, such that the stress at a point is given by

$$\boldsymbol{\sigma} = \mathbb{D} \left(\boldsymbol{\varepsilon} - \boldsymbol{\varepsilon}_p^{(t)} - \dot{\boldsymbol{\varepsilon}}_p \Delta t \right), \quad (1)$$

where $\boldsymbol{\sigma}$, $\boldsymbol{\varepsilon}$, and $\dot{\boldsymbol{\varepsilon}}_p$ are the stress, total strain, and plastic strain rate, respectively, at time $t + \Delta t$; $\boldsymbol{\varepsilon}_p^{(t)}$ is the plastic strain at time t ; Δt is the time increment, and \mathbb{D} is the elasticity tensor. A viscoplastic flow rule relates the stress to the plastic strain rate:

$$\dot{\boldsymbol{\varepsilon}}_p = \dot{\gamma}_0 \sum_{s=1}^{N_s} \mathbf{m}_s \left(\frac{|\mathbf{m}_s : \boldsymbol{\sigma}|}{g_s} \right)^m \text{sgn}(\mathbf{m}_s : \boldsymbol{\sigma}), \quad (2)$$

where s is a slip system identifier, N_s is the total number of slip systems, $\dot{\gamma}_0$ is a reference strain rate, m is the inverse rate sensitivity, and \mathbf{m}_s and g_s are the Schmid tensor and critical resolved shear stress (CRSS), respectively, for slip system s . The model uses the twelve $\{111\}\langle 1\bar{1}0 \rangle$ octahedral slip systems typical of face-centered cubic materials.

For the calibration study, it was desired to use a relatively simple hardening law that still demonstrated interesting behavior and had approximate ground-truth values and intervals for each parameter in prior work (Bandyopadhyay et al., 2019). To this end, a basic hardening/dynamic recovery model (similar to Armstrong-Frederick-type hardening laws) was chosen:

$$\dot{g}_s = (H - H_d g_s) \sum_{s=1}^{N_s} |\dot{\gamma}_s|, \quad g_s = g_0 + \int_0^t \dot{g}_s dt, \quad (3)$$

where g_0 is the initial CRSS on all slip systems, H is the hardening coefficient, and H_d is the dynamic recovery coefficient. The self and latent hardening coefficients are assumed to be unity.

2.2. Model geometry and boundary conditions

The microstructure for the simulations was taken from the open-source dataset of Stinville et al. (2022), which contains 3-D microstructural information for a $549 \mu\text{m} \times 526 \mu\text{m} \times 420 \mu\text{m}$ sample of Inconel 718. An inverse pole figure (IPF) map of the microstructure is shown in Fig. 2a. The microstructure has a 1- μm voxel size, one free surface, and a large number of annealing twins. To make the computations in this study more tractable, several simplifications to the microstructure were made: 30 voxels were removed from the $-y$ face to eliminate the free surface, the voxel size was coarsened to 5 μm , twins were merged into their parent grains, and a $64 \times 64 \times 64$ -voxel region was cut out for use in the simulations. An IPF map of the result is shown in Fig. 2b. Finally, a buffer region with a thickness of 6 voxels was added on the y and z faces. The buffer was assigned an isotropic elastic and perfectly plastic material model, such that the microstructure approximates a smaller region within the bulk of a tensile specimen.

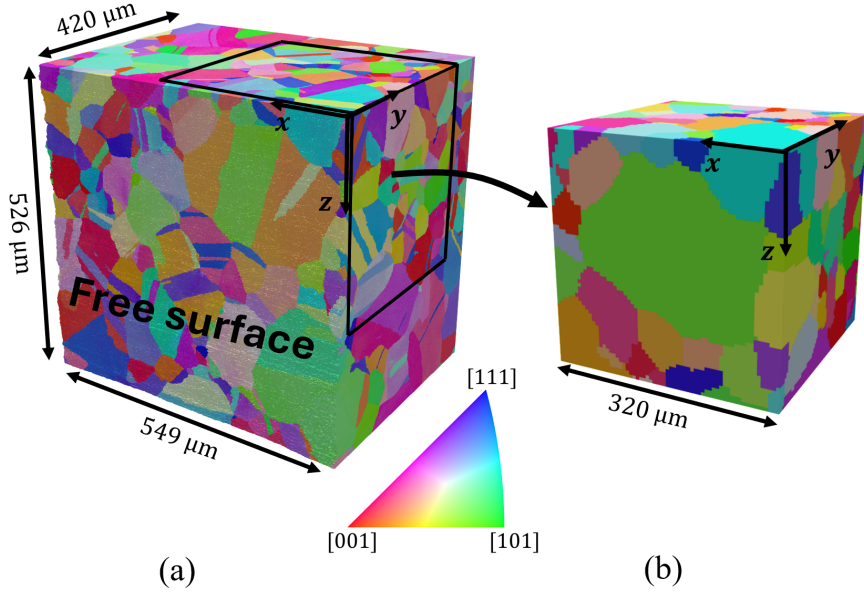


Figure 2: IPF maps of (a) the full microstructure, reconstructed from the data in Stinville et al. (2022), and (b) the simplified microstructure used in the simulations. The reference direction is the x direction for both IPF maps. The black-outlined region in (a) corresponds to the microstructure in (b).

Table 1: Fixed material parameters.

Material region	Symbol	Value
Microstructure	C_{11}	242.2 GPa
	C_{12}	138.9 GPa
	C_{44}	104.2 GPa
	$\dot{\gamma}_0$	0.004 s^{-1}
Buffer region	E	140.9 GPa
	μ	104.2 GPa
	σ_Y	300 MPa

Material parameters that were fixed are shown in Table 1. These include the elastic constants (C_{11} , C_{12} , and C_{44}) (Ghorbanpour et al., 2017) and reference strain rate (Bandyopadhyay et al., 2019) in the microstructure and all properties of the buffer material (Young’s modulus, E ; shear modulus, μ ; and yield stress, σ_Y). To minimize the influence of the buffer on the uniaxial behavior of the microstructure while still providing some constraint, the buffer was chosen to be more compliant and have a lower yield stress than the microstructure. Specifically, Young’s modulus and the shear modulus were chosen as the directional stiffness and directional shear modulus of the microstructural elasticity tensor in the crystal coordinate directions. The yield stress was chosen such that it would be below the global yield stress across all parameter combinations.

In each simulation, a constant mean strain rate was applied in the x direction up to 1% strain. The mean strain rate was set equal to the reference strain rate in Table 1. The mean stress for all other components was fixed to zero. Details on how the boundary conditions² were enforced on the periodic domain are given in Appendix B.

3. Calibration approach

3.1. Calibration as a Bayesian inference problem

The goal of the calibration is to quantify uncertainty in a set of calibration parameters, $\boldsymbol{\theta} \in \mathbb{R}^p$, given noisy measurement data, $\mathbf{y} \in \mathbb{R}^q$. Here, p is the number of parameters to be calibrated, and q is the number of experimentally measured output quantities (e.g., number of points on a stress-strain curve). A Bayesian perspective is adopted in this study, meaning the output of the calibration is a joint probability distribution over the model parameters reflecting the analyst’s belief about their true values after observing data. This distribution is referred to as the posterior and, from Bayes’ theorem, has probability density function (PDF)

$$p(\boldsymbol{\theta}|\mathbf{y}) = \frac{p(\mathbf{y}|\boldsymbol{\theta})p(\boldsymbol{\theta})}{Z}, \quad (4)$$

where $p(\mathbf{y}|\boldsymbol{\theta})$ is the likelihood function, $p(\boldsymbol{\theta})$ is the prior PDF for the parameters, and Z is a normalizing constant referred to as the marginal likelihood or model evidence.

The likelihood function quantifies the plausibility of observing \mathbf{y} if $\boldsymbol{\theta}$ were the true parameter values. Its definition depends on the assumed relationship between the data, the model, and the noise,

$$\mathbf{y} = \mathcal{M}(\boldsymbol{\theta}) + \boldsymbol{\epsilon}, \quad (5)$$

where $\mathcal{M}(\cdot)$ is the model and $\boldsymbol{\epsilon} \sim \mathcal{N}(0, \Sigma)$ is zero-mean Gaussian measurement noise. The Gaussian noise assumption produces a closed-form likelihood, which enables direct evaluation of the posterior PDF up to

²Strictly speaking, in spectral methods, conventional boundary conditions cannot be enforced without modifying the algorithm, due to the inherent periodicity. Rather, the *global mean* stress and strain components must be specified.

some proportionality $p(\boldsymbol{\theta}|\mathbf{y}) \propto p(\mathbf{y}|\boldsymbol{\theta})p(\boldsymbol{\theta})$ for any vector $\boldsymbol{\theta}$. This is critical for performing the calibration as it allows for random walk algorithms to be employed that can produce samples from the posterior without knowing Z , as will be discussed in Section 3.4. For most cases, a constant variance was assumed for each measurement such that $\Sigma = \mathbf{I}\sigma_{\text{noise}}^2$. One adjustment to this approach is explored in Section 4.3.

3.2. Calibration parameters

Four material parameters were initially selected for the calibration study: the inverse rate sensitivity, m ; the initial CRSS, g_0 ; and the hardening and dynamic recovery coefficients, H and H_d , respectively. However, some caution is required. The hardening model in this study has a saturation stress, g_1 , that is found by setting the hardening rate to zero in Eq. (3) and solving for g_s :

$$g_1 = H/H_d. \quad (6)$$

Strain hardening occurs if $g_1 > g_0$, while strain softening occurs if $g_1 < g_0$, as visualized in Fig. 3. Sampling independently from prior distributions on H and H_d may lead to a situation where $g_1 \ll g_0$ and sudden, extreme softening occurs immediately after the yield point. This behavior is both nonphysical for the material of interest and causes numerical problems in the solver. Therefore, the ratio g_0/g_1 was used as a calibration parameter instead of H_d , providing three intuitive characteristics:

1. Strain hardening occurs if $g_0/g_1 < 1$. The amount of hardening increases as the ratio approaches zero.
2. Strain softening occurs if $g_0/g_1 > 1$. The amount of softening increases as the ratio increases.
3. Perfectly plastic behavior occurs if $g_0/g_1 = 1$.

An upper bound on the support of prior distribution for g_0/g_1 restricted the maximum amount of softening that could occur.

Following standard practice for calibration experiments where the noise level is unknown, σ_{noise} is included in the set of calibration parameters. The vector of calibration parameters was therefore

$$\boldsymbol{\theta} = [m, g_0, H, g_0/g_1, \sigma_{\text{noise}}], \quad (7)$$

so the number of parameters was $p = 5$. When data is available from multiple experiments as is the case for the multiscale calibration presented here, separate noise levels for each measurement type can be estimated as appropriate. An example of this case is analyzed in Section 4.3.

Independent uniform priors were placed on each parameter based on the ranges considered in Bandyopadhyay et al. (2019). This means that, prior to observing data, it is assumed that all values within the prior bounds are equally likely to be the true value. Prior bounds are shown in Table 2.

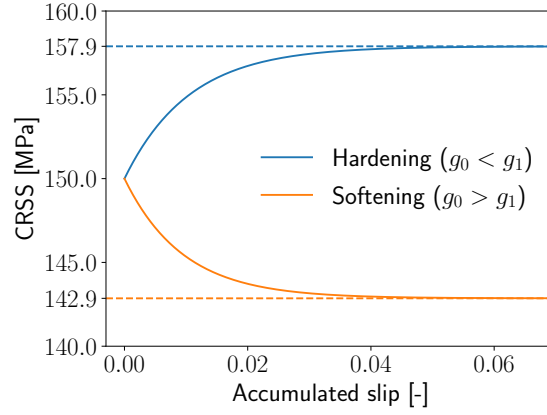


Figure 3: Examples of cases where strain hardening and strain softening occur. Both curves have $g_0 = 150$ MPa and $H = 15,000$ MPa. The blue hardening curve has $H_d = 95$, resulting in $g_1 \approx 157.9$ MPa. The orange softening curve has $H_d = 105$, resulting in $g_1 \approx 142.9$ MPa.

Table 2: Ground-truth values and bounds for the uniform priors on the calibration parameters.

Parameter	Lower bound	Upper bound	Ground truth
m	5	25	10
g_0	300 MPa	700 MPa	400 MPa
H	1000 MPa	30,000 MPa	10,000 MPa
g_0/g_1	0.0	1.5	0.8
σ_{noise}	0 MPa	100 MPa	5 MPa

3.3. Calibration data

Synthetic measurement data was generated by a single CP simulation with fixed ground-truth parameter values, again based on (Bandyopadhyay et al., 2019) and provided in Table 2. The global data consists of the mean stress in the loading direction at 13 time points during the simulation. The 13 time points correspond to mean loading direction strains of 0.3%, 0.4%, 0.425%, 0.45%, 0.475%, 0.5%, 0.55%, 0.6%, 0.65%, 0.7%, 0.8%, 0.9%, and 1.0%. The strains were chosen such that there is a higher density of data near the onset of global yielding. The local data consists of grain-average stresses in the loading direction at the same 13 time points for 32 grains, resulting in 416 total local data points. The 32 grains are all at least 5 voxels from any edge of the microstructural region and have a volume of at least 20 voxels. These selection criteria were intended to mimic grain selection in HEDM experiments (Menasche et al., 2021). Finally, the mean and grain-average stresses were polluted with zero-mean noise sampled from a Normal distribution with standard deviation $\sigma_{\text{noise}} = 5$ MPa. The resulting dataset was used as the measurement data for all calibrations in this study, with some modifications to the noise and availability of the local data in Section 4.3.

The synthetic data generated from the CP model, including the calibration data and the training data for the surrogate model, is summarized in Fig. 4. For the mean stresses, the ground-truth data (before adding the noise) and the calibration data (after adding the noise) are both shown. For clarity, only the ground-truth grain-average stresses are shown. The surrogate model training is described further in Section 4.1.

3.4. Sequential Monte Carlo

Eq. (4) cannot be evaluated directly due to the unknown normalizing constant Z , which makes it difficult to compute posterior quantities. Thus, a common approach is to draw samples from the posterior using random walk algorithms such as MCMC. As discussed in Section 1, sampling methods are often intractable when calibrating full-field CP models. In a standard MCMC algorithm, each proposed sample requires an evaluation of the model to compute $p(\mathbf{y}|\boldsymbol{\theta})$ prior to accepting or rejecting the sample. Each evaluation is completed sequentially due to the Markov nature of the random walk. To overcome this computational burden, SMC, a parallelizable alternative to MCMC, was adopted. Key aspects of the SMC algorithm are described here. A more detailed description of SMC, its variants, and convergence properties can be found in Del Moral et al. (2006, 2012); Leser et al. (2018).

The computational advantage of SMC is derived from its use of a population of independent, weighted parameter vectors called “particles”. The particles are initially sampled directly from the prior and then evolved through a series of intermediate target distributions via successive sequential importance sampling and resampling steps. The target distributions are defined using likelihood annealing, such that the i^{th} target is $p_i(\boldsymbol{\theta}|\mathbf{y}) \propto p(\mathbf{y}|\boldsymbol{\theta})^{\phi_i} p(\boldsymbol{\theta})$. The exponent ϕ_i monotonically increases with $\phi_i \in [0, 1]$, such that the first target is simply the prior and the last target is the posterior. Transitioning the particles from one target distribution to the next is referred to as an SMC step.

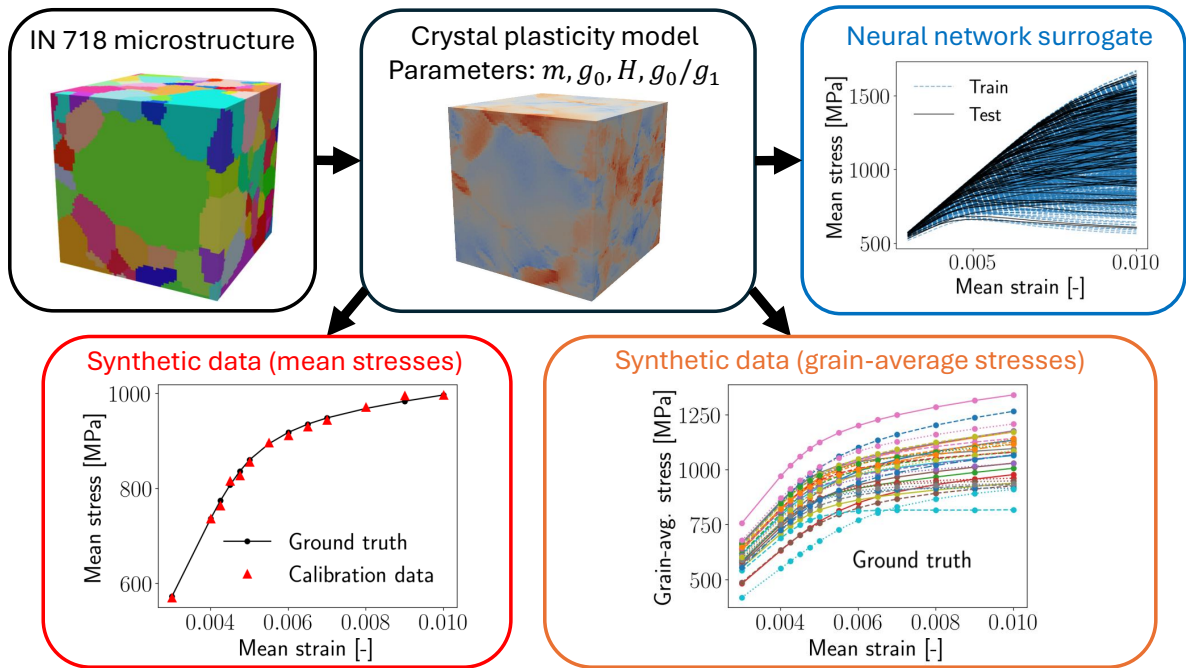


Figure 4: Summary of the CP model setup (black boxes) and data generated for use in the calibration. The training and test data for the surrogate model (blue box) consists of the mean stresses from 1000 simulations with material parameters sampled from the uniform prior distributions. The synthetic measurement data is from a simulation with $m = 10$, $g_0 = 400$ MPa, $H = 10,000$ MPa, and $g_0/g_1 = 0.8$, with zero-mean noise added to both the mean stresses (red box) and the grain-average stresses (orange box). The mean stresses are shown before and after adding the zero-mean noise. For clarity, the grain-average stresses are shown prior to adding the noise.

For each target distribution, importance weights, w_j , are assigned to the j^{th} particle,

$$w_j \propto \frac{p(\boldsymbol{\theta}_j)p(\mathbf{y}|\boldsymbol{\theta}_j)^{\phi_i}}{p(\boldsymbol{\theta}_j)p(\mathbf{y}|\boldsymbol{\theta}_j)^{\phi_{i-1}}} = p(\mathbf{y}|\boldsymbol{\theta}_j)^{\phi_i - \phi_{i-1}}. \quad (8)$$

Resampling with replacement then occurs to move low-weight particles to high-weight regions of the parameter space. Over the course of several SMC steps, particles will therefore be moved toward regions of high posterior probability density. However, this resampling approach often produces a degenerate population with most particles resampled to a small subset of the original population, resulting in very few unique values of $\boldsymbol{\theta}$. The reason is that the support of the prior distribution is typically much broader than the posterior distribution. To mitigate degenerate populations, each SMC step includes a short MCMC run for each particle, enabling local exploration of the i^{th} target distribution via random walk. In summary, each SMC step involves computing the importance weights, resampling the particles, and completing an MCMC run for each particle.

SMC steps are carried out for each target until termination of the algorithm at $\phi_i = 1$. The end result is similar to MCMC in that the final particle population represents samples from the posterior distribution. However, all particles are moved independently, meaning that evaluations of the likelihood within each short MCMC run can be parallelized across particles. This results in significant speedup that scales well with additional computational resources.

The SMC computations in this study were completed using the open-source SMCPy code³ developed at NASA Langley Research Center. For all computations, five MCMC proposals were used per particle per SMC step. The number of particles varied depending on computational cost and will be provided along with the relevant results. SMCPy’s `AdaptiveSampler` class was used, meaning each ϕ_i was selected adaptively such that the resampled population met a target effective sample size, defined as the percentage of particles with meaningful importance weights. This avoided additional hyperparameters to define the target sequence while ensuring target distributions evolved gradually enough to avoid sampling errors. The tradeoff was that the total number of SMC steps and thus the total walltime of each calibration was not known in advance.

3.5. Two-stage calibration

A goal of the two-stage calibration in this study is to increase computational efficiency of SMC with the full-field CP model relative to a single-stage calibration. The computational cost of the calibration is a function of the number of likelihood evaluations, each of which involves a CP simulation. The number of likelihood evaluations in turn depends on the number of SMC steps required for convergence of the algorithm at $\phi = 1$. Specifically, the five MCMC proposals correspond to five likelihood evaluations per particle per SMC step. More SMC steps are typically required if the prior distribution is uninformative or

³Available at <https://github.com/nasa/SMCPy>.

minimally informative, typically meaning that it has a much wider distribution of probability mass than the posterior distribution. Therefore, using informative priors that place the initial particle population closer to the posterior could reduce the computational cost of the SMC procedure.

The goal of the first stage was to infer a set of preliminary posterior distributions that are in turn used as informative priors for the second stage. The first stage was computationally cheap due to using the neural network surrogate model, which has negligible cost to evaluate relative to the full-field CP model. On the other hand, there is a risk that the informative priors will be overconfident and biased (i.e., tightly distributed about an incorrect parameter value) due to bias in the surrogate model. To help avoid this issue, only the global data was used in the first stage: the training data for the neural network surrogate came from the mean stresses in a set of CP simulations, and only the mean stresses were provided as measurement data in the SMC calibration. Thus, the number of measurement points for the first stage was $q = 13$.

A kernel density estimate (KDE) of the joint posterior distribution of the material parameters from the first stage was used as the prior for the material parameters in the second stage. Since one calibration case considered different noise for the mean strains and grain-average strains, the original uniform prior was still used for the noise standard deviation in the second stage to enable fair comparisons between the different calibrations. The full synthetic dataset of mean and grain-average stresses was used as measurement data for the second stage, resulting in $q = 429$ measurement points. The computational efficiency of the two-stage procedure is quantified by comparing walltime and the number of SMC steps with one-stage calibrations in Section 4.4. Refer to Fig. 1 for a visual summary of the overall two-stage calibration procedure.

4. Results

Results are first presented for the surrogate model for the mean stresses, including trends in the training and test samples from the CP model. These samples provide insight into the model behavior and some possible challenges for both the surrogate model and the calibration. Then, posterior distributions are presented for each stage in the two-stage calibration procedure to study the influence of local data on the inferred parameter values and associated uncertainty. The second stage in the calibration is repeated with different restrictions on the local data to examine the robustness of the calibration procedure to more realistic data. Finally, the two-stage procedure is compared with several one-stage approaches to study tradeoffs for computational cost and calibration accuracy and precision.

Throughout this section, the marginal and joint posterior distributions from each calibration are primarily visualized and compared using histograms. Summary statistics for all the marginal posterior distributions are also provided in Appendix D to assist with more quantitative comparisons.

Table 3: Grid search values for parameters in the neural network surrogate model, with optimal values bolded.

Parameter	Grid search values
Hidden layer sizes	$[(50,), (100,), (50, 50), (100, 50), (\mathbf{100}, \mathbf{100})]$
α	$[\mathbf{10}^{-1}, 10^{-2}, 10^{-3}, \dots, 10^{-7}]$
η	$[10^{-1}, 10^{-2}, \mathbf{10}^{-3}, 10^{-4}]$

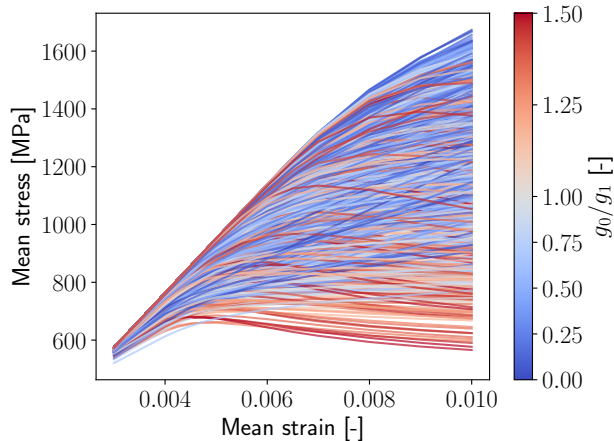


Figure 5: Mean stress-strain curves at the 13 time points of interest for the 1000 simulations from Latin hypercube samples of the four material parameters used to train and test the neural network surrogate model. The curves are colored such that red indicates $g_0/g_1 > 1$ and blue indicates $g_0/g_1 < 1$ to highlight the different curve shapes.

4.1. Sensitivity study and surrogate model training

For the two-stage calibration procedure, a neural network surrogate model (specifically, the multilayer perceptron in `scikit-learn` (Pedregosa et al., 2011)) was trained to map the four calibration parameters to the 13 global mean stresses. To generate the training data, CP simulations were completed using 1000 Latin hypercube samples within the bounds of the independent uniform prior distributions on the four material parameters (see Section 3.2). The data was split into a set of 900 training samples and 100 test samples. Trends in the training and test data are analyzed first.

Mean stress-strain curves at the 13 time points of interest for the 1000 Latin hypercube samples are shown in Fig. 5. At lower strains, all simulations are in the elastic regime or in the initial stages of global yielding. The curves start to diverge from one another as plasticity sets in at higher strain values. Samples with softening ($g_0/g_1 > 1.0$) have a downward slope after yielding begins and are particularly noticeable for low stress values at 1.0% strain.

To further analyze the relationship between the mean stresses and the calibration parameters, the mean stresses at 0.4%, 0.6%, 0.8%, and 1.0% mean strain are extracted for each simulation. The pairwise plots in

Fig. 6 show correlations between these four mean stresses and the material parameters. The main finding from the pairwise plots is that all stresses are strongly correlated with the initial CRSS. Other first-order correlations are relatively weak. By controlling the initial yield point, the initial CRSS essentially scales the stress-strain curves in the plastic regime up or down. The ratio g_0/g_1 is related to the strength of the dynamic recovery term and is weakly correlated with the stress at 1.0% strain. Meanwhile, a lower value of the inverse rate sensitivity allows yielding to begin at lower stresses, shown through the correlation between m and the stress at 0.4% strain. Overall, however, the lack of clear correlations between the mean stresses and parameters other than the initial CRSS suggest that uniqueness challenges may arise in the calibration.

With the training data in hand, the surrogate was trained using the Adam optimizer and an adaptive learning rate with rectified linear unit (RELU) activation functions. To minimize effects of feature scaling, the training data was scaled to zero mean and unit variance. Optimal hyperparameters of the surrogate were found using a grid search with five-fold cross-validation on the training set. The hyperparameters included in the grid search were the number and size of the hidden layers; α , a weight parameter for the L2 regularization term that limits overfitting; and η , the initial learning rate. Values of each parameter included in the grid search are based on the `scikit-learn` documentation and examples and are given in Table 3. Using the optimal hyperparameters, the model was then trained on the entire training set and evaluated on the test set.

Due to the scaling effect of the initial CRSS, the stresses at each strain value are correlated with each other. However, the neural network surrogate assumes that all output quantities are independent. Thus, rather than using the stresses directly, the surrogate was trained using the first four principal components (PCs) of the stresses from the training data, determined using principal component analysis (PCA). The first four PCs explain more than 99.9% of the variance in the mean stress data. Using the PCs was also found to eliminate occasional convergence issues for some parameter combinations in the grid search and to produce stress-strain curves with more realistic shapes. Details on the PCA can be found in Appendix C. The optimal hyperparameters from the grid search were two hidden layers with sizes (100, 100), $\alpha = 0.1$, and $\eta = 0.001$. Using the optimal hyperparameters, the root-mean-squared error was 5.42 MPa on the training set and 5.37 MPa on the test set (about 0.6% of the global yield stress from the ground-truth simulation of approximately 900 MPa), suggesting that overfitting was avoided.

4.2. Two-stage global-local calibration

The first stage required 14 SMC steps and only about 10 seconds on a laptop computer to generate 40,000 posterior samples using the surrogate model due to the efficiency of the surrogate. The second stage was completed on the NASA Langley K-cluster, using 644 CPU cores across 23 Intel E5-2697 V3 nodes. Each core was assigned two particles in the SMC algorithm, resulting in 1288 total posterior samples. As noted in Section 3.4, one SMC step required five model evaluations per particle and therefore ten total evaluations

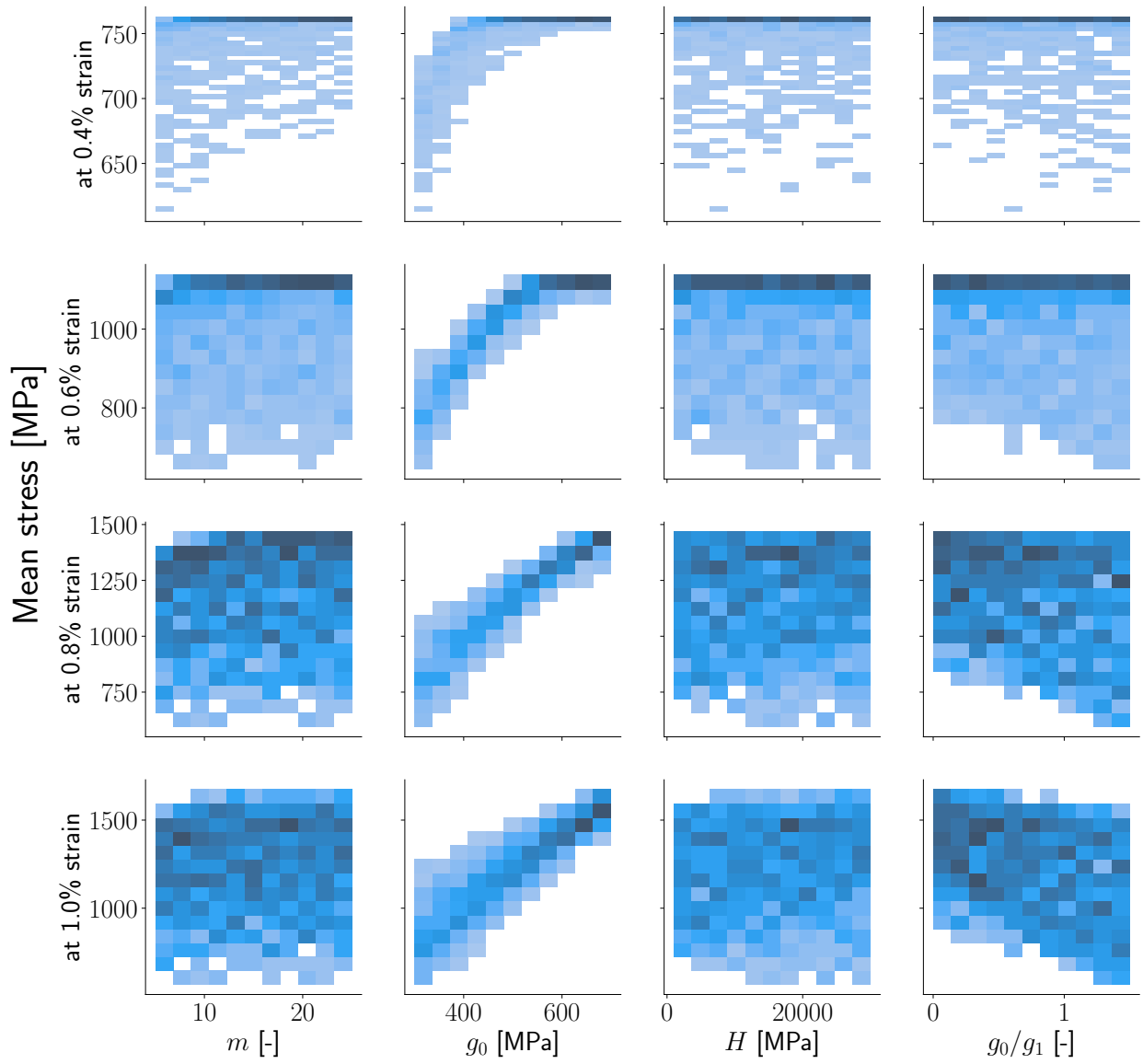


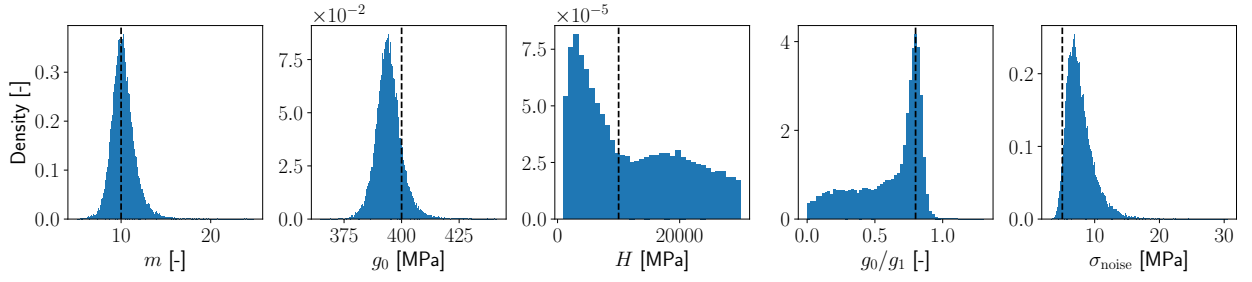
Figure 6: Pairwise plots of the material parameters and the mean stresses at mean strains of 0.4%, 0.6%, 0.8%, and 1.0% in the 1000 Latin hypercube samples. The stresses are strongly correlated with g_0 , while first-order correlations with other parameters appear to be weak.

on each core. The second stage required 18 SMC steps and a total of over 100,000 CP simulations, with a total walltime of about 90 hours and total CPU time of about 2400 days. This computation would be intractable without the parallelization enabled by the SMC algorithm.

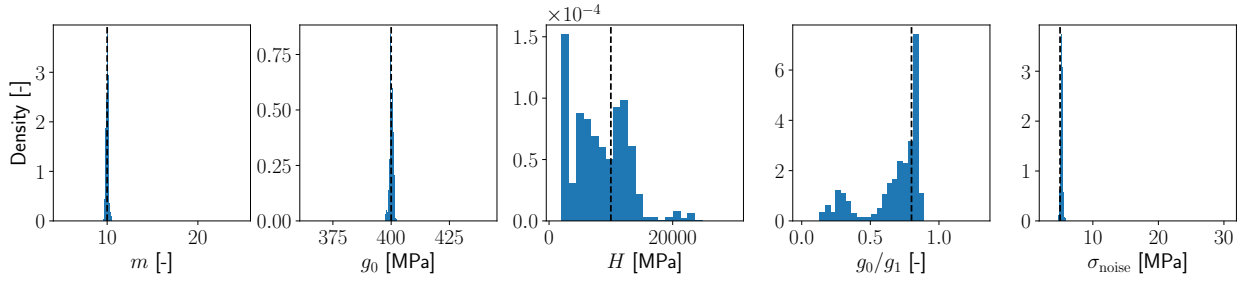
Marginal posterior distributions from both stages are shown in Fig. 7. In the first stage (Fig. 7a), m and g_0 appear to be reasonably well calibrated. Both have approximately Normal distributions centered close to the ground-truth value. However, there is some bias in the posterior distribution for g_0 , and some samples of m are close to the upper bound of the prior and far from the ground-truth value. On the other hand, calibration of H and g_0/g_1 appears to be more challenging. Although the mode of the distribution (or maximum a posteriori estimate) for g_0/g_1 is close to the ground-truth value, the posterior distributions for both H and g_0/g_1 span essentially the entire parameter space. Samples with slip-system-level softening behavior ($g_0/g_1 > 1.0$) are mostly, but not entirely, eliminated. Finally, the posterior distribution for the scale of the noise, σ_{noise} , is biased above the ground-truth value of 5 MPa, and the upper tail extends to significantly larger values. This bias indicates that the noise term is compensating for discrepancy between the model and the data-generating process.

Posterior distributions after the second stage (Fig. 7b and c) show significantly reduced uncertainty for m and g_0 , forming a tighter distribution centered on the ground-truth values relative to the first stage. Uncertainty is also somewhat reduced for H and g_0/g_1 . In particular, samples with softening are completely eliminated: the maximum value of g_0/g_1 across the 1288 posterior samples is about 0.89. However, the distributions for H and g_0/g_1 both appear to be bimodal, and the posterior samples include values of H from across almost the entire parameter space. This suggests that obtaining point estimates of H and g_0/g_1 remains challenging, even with both global and local calibration data. Finally, the bias and uncertainty in the posterior distribution for σ_{noise} are both significantly reduced, reflecting the use of the full CP model rather than the biased surrogate.

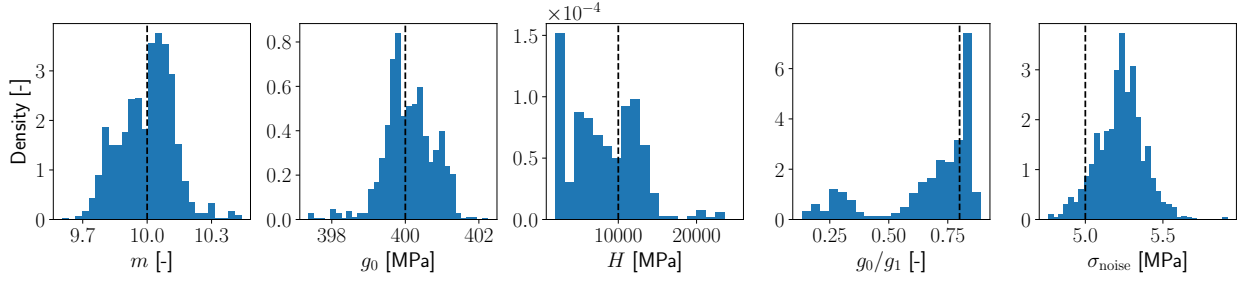
To obtain further insight into the posterior distributions of H and g_0/g_1 , pairwise plots for these parameters after stage one and stage two are shown in Fig. 8a and Fig. 8b, respectively. The off-diagonal joint distributions in each plot demonstrate an interesting correlation structure, which becomes stronger after the second stage. The joint distribution in Fig. 8b has one mode close to the ground-truth values of both parameters. However, the shape of the distribution suggests that a range of H values surrounding the ground-truth is consistent with the data for $g_0/g_1 \approx 0.8$. There is also a second mode of the distribution at small values of H , where a range of g_0/g_1 values appears to be consistent with the data. Finally, the sharp drop-off in the distribution as g_0/g_1 approaches 0.9 suggests that the calibration may have located an upper bound for this parameter below 1.0, due in part to the minimal uncertainty about g_0 . Essentially, a too-high value of g_0/g_1 would cause the grain-average stresses to saturate before reaching stress values seen in the data, regardless of the value of H .



(a) First stage (surrogate with mean stresses only).



(b) Second stage (CP model with mean and grain-average stresses).



(c) Second stage, with tighter horizontal axis limits to more clearly show the distributions.

Figure 7: Marginal posterior distributions for the five calibration parameters from each stage in the two-stage calibration. The dashed lines represent the ground-truth values of the parameters.

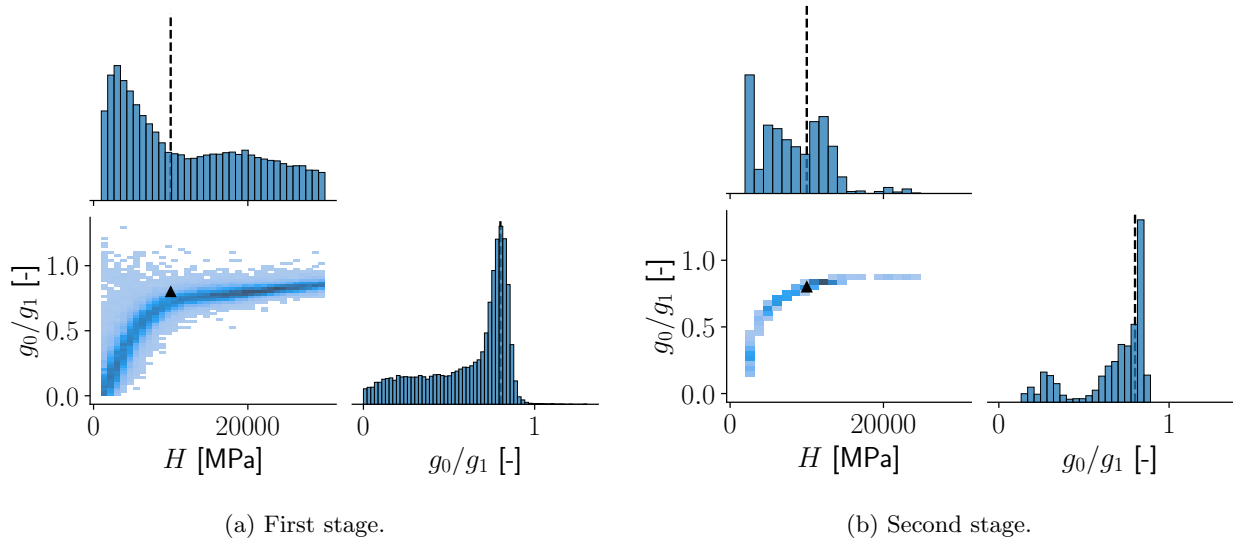


Figure 8: Pairwise plots for the posterior distributions of H and g_0/g_1 after the first and second calibration stages. Black dashed lines in the marginal distributions along the diagonals and black triangles in the joint distributions represent the ground-truth values.

4.3. Two-stage calibration with more realistic grain-average stress data

The results in the previous section represent an ideal situation where grain-average stress data is available at the same time points and the same noise level as the global mean stress. In reality, estimating grain-average stresses from HEDM measurements is significantly more expensive than measuring the mean stress with a load cell and requires pausing the test at each point of interest. The HEDM data also may be influenced by more sources of noise and uncertainty than the mean stress measurement. Therefore, the second stage of the calibration was repeated twice to study the influence of more realistic data constraints.

First, calibration data for the grain-average stresses was made available only for mean strains of 0.4%, 0.6%, 0.8%, and 1.0% (i.e., there are only 4 grain-average stress values for each of the 32 grains of interest, resulting in 128 total local data points). As a result, there were 128 grain-average stress points and $q = 141$ total measurement points. The Air Force Research Laboratory (AFRL) additive manufacturing modeling challenge had similar constraints on the amount of HEDM grain-average stress data collected in the plastic regime (Menasche et al., 2021). This case is referred to as the “reduced grain stresses” case.

Second, the standard deviation of the noise added to the grain-average stress measurements was doubled to 10 MPa. This case is referred to as the “increased noise” case. The variance of the noise term in the likelihood function, Eq. (5), was modified such that $\Sigma_{1:13,1:13} = \mathbf{I}_{13 \times 13} \sigma_{\text{noise,global}}^2$ for the 13 mean stress data points and $\Sigma_{14:429,14:429} = \mathbf{I}_{416 \times 416} \sigma_{\text{noise,local}}^2$ for the 416 grain-average stress data points. Both $\sigma_{\text{noise,global}}$ and $\sigma_{\text{noise,local}}$ were included as calibration parameters with the same uniform priors and ground-truth values of $\sigma_{\text{noise,global}} = 5$ MPa and $\sigma_{\text{noise,local}} = 10$ MPa. Note that the grain-average stresses at all 13 original time

points were made available to the calibration in the increased noise case. Thus, the number of calibration parameters was $p = 6$, and the number of measurement points was $q = 429$.

Fig. 9 shows a comparison between the marginal posterior distributions for the two new cases and the results shown in Section 4.2 at the end of the two-stage calibration. For m and g_0 , the calibration procedure is fairly robust to reduced data and increased noise. The uncertainty is similar across all three cases, although some bias is introduced in the reduced grain stresses case. The increased noise case does not have this bias, suggesting that the quantity of local measurements may be more important than the precision of those measurements. The posterior distributions for H and g_0/g_1 in the two new cases still eliminate samples at large values of both parameters. However, the posterior distributions for H in particular have notable bias towards values below the ground truth. The strong correlation between H and g_0/g_1 observed in Fig. 8b is also still present in the joint posterior distribution. As before, the ground truth value lies in the support of the joint posterior distribution for both the reduced grain stresses and increased noise cases, even though point estimates from the marginal distributions of H and g_0/g_1 would be biased.

4.4. Alternative one-stage calibration approaches

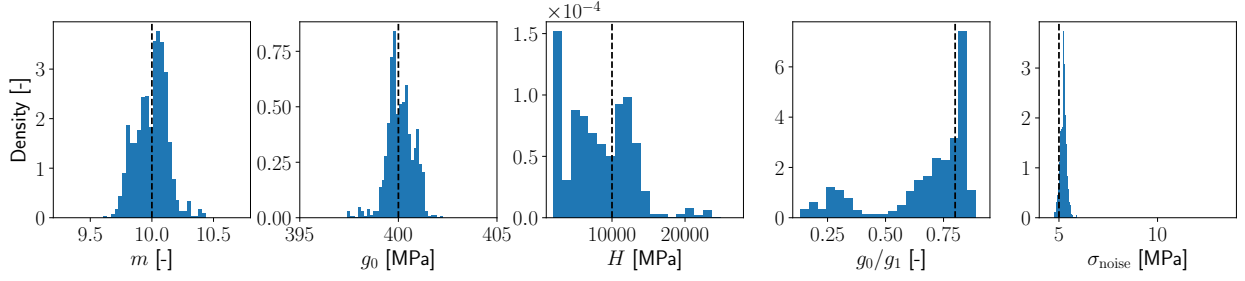
To assess the advantages and limitations of the proposed two-stage calibration, it is interesting to compare the results with several one-stage calibrations. To this end, three one-stage calibrations, using the uniform priors in Table 2, are presented here:

1. Calibration using the CP model but with only the mean stresses as calibration data (identical to stage one in the two-stage calibration but with the CP model instead of the surrogate).
2. Calibration using the CP model with both mean and grain-average stresses (identical to stage two in the two-stage calibration but with uniform priors).
3. Calibration using a surrogate trained on the first six PCs of the full dataset of both mean and grain-average stresses from the Latin hypercube samples. The training procedure was identical to the one described in Section 4.1.

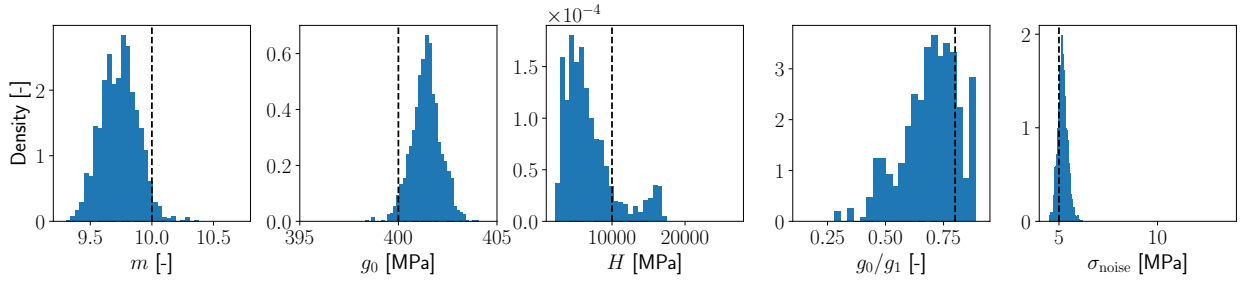
Marginal posterior distributions from the three one-stage approaches are shown in Fig. 10. To help with comparisons, the marginal posterior distributions from the original two-stage calibration are shown again in Fig. 7d.

The posterior distributions for the CP model with mean stresses only (Fig. 10a) demonstrate the limitations of using only global data. There is more uncertainty in the distributions for m and g_0 than in any of the two-step calibration results. No samples have $g_0/g_1 > 1$, but the distributions for both H and g_0/g_1 still span most of the parameter space.

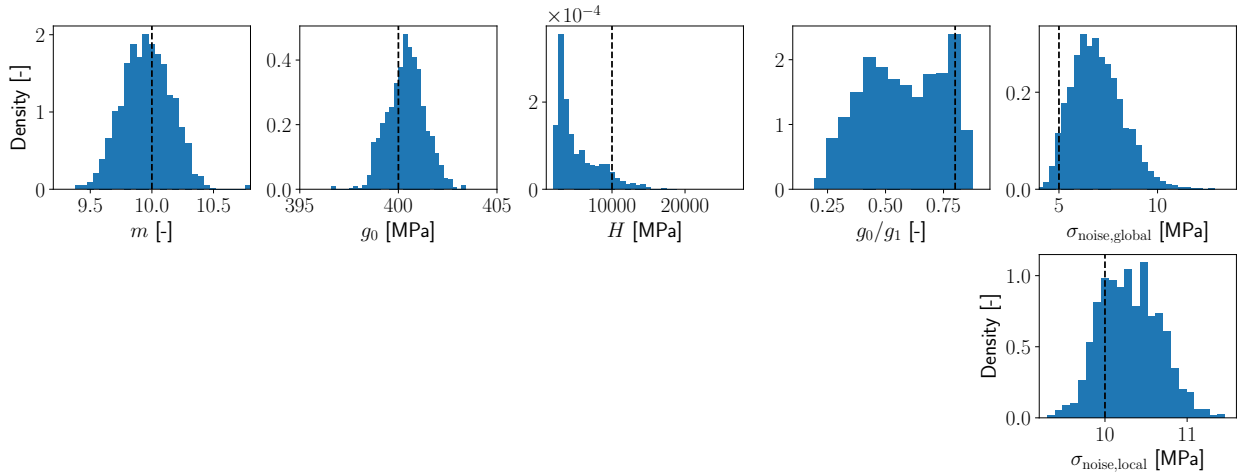
The posterior distributions for the CP model with both mean and grain-average stresses (Fig. 10b) are very similar to the end of the two-stage calibration. Both approaches should converge to the same result



(a) Two-stage calibration with all stress data and equivalent global and local noise (same data as in Fig. 7bc).

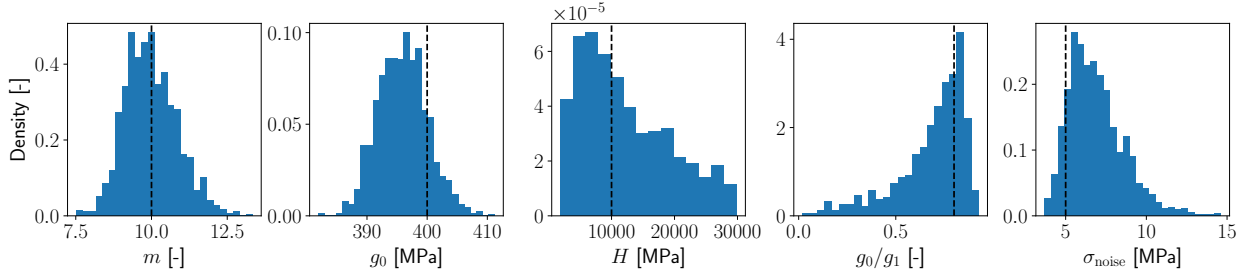


(b) Reduced grain stresses case.

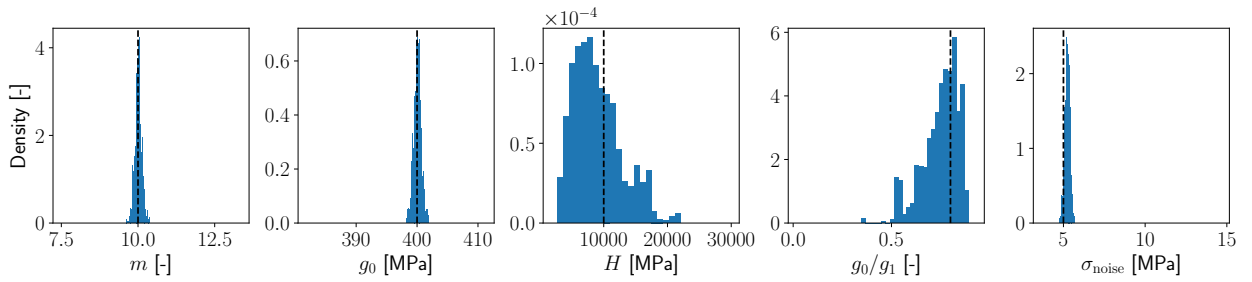


(c) Increased noise case.

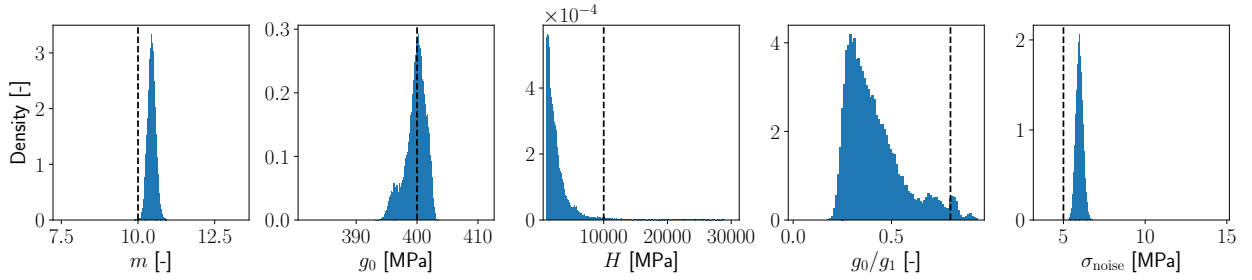
Figure 9: Marginal posterior distributions for the five calibration parameters from the two-stage calibration with different constraints on the grain-average stress data.



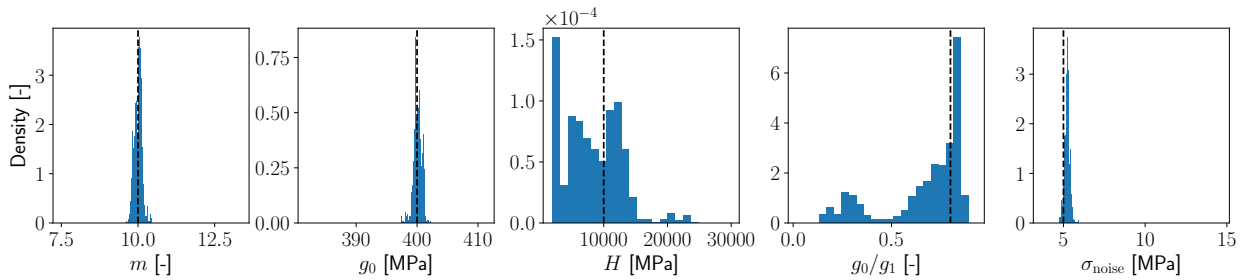
(a) CP model with only mean stresses.



(b) CP model with mean and grain-average stresses.



(c) Surrogate model with mean and grain-average stresses.



(d) Two-stage calibration with mean and grain-average stresses (same data as in Fig. 7bc).

Figure 10: Marginal posterior distributions for the five calibration parameters from the three one-stage calibration procedures described in Section 4.4. All cases use the same horizontal axis bounds. A comparison with the two-stage calibration is also included in (d).

in the limit of a large amount of calibration data since the only difference between the two calibrations is the priors: uniform priors for Fig. 10b and posteriors from the first stage for Fig. 10d. The most significant difference in the posterior distributions is that the second mode at small values of g_0/g_1 and H is largely absent in Fig. 10b. The one-stage calibration with the CP model required 22 SMC steps and about 7.5 days, compared to 18 SMC steps and about 3.75 days for the two-stage calibration using the same computing resources.

Finally, Fig. 10c shows the posterior distributions for a surrogate model trained on both the mean and grain average stresses. The surrogate model was trained using the same strategy as in Section 4.1; here, the first six PCs explained greater than 99.9% of the variance. The root-mean-squared error was 5.94 MPa on the training data and 5.96 MPa on the test data (about 0.7% of the approximate global yield strength from the ground-truth simulation). While this result suggests that overfitting was again avoided, the error is about 10% higher than in the surrogate for the mean stresses only. In the posterior distributions, the uncertainty in m , g_0 , and σ_{noise} is generally comparable to the calibrations using both mean and grain-average stresses (Fig. 10bd). However, the distributions for m , H , g_0/g_1 , and σ_{noise} are all significantly biased in Fig. 10c, even though the error on the test set did not indicate any serious problems with the surrogate in an average sense. Using a surrogate model for the mean and grain-average stresses thereby highlights both the advantages of including local data (e.g., reduced uncertainty) and the challenges of using a surrogate (e.g., possible bias in the model).

5. Discussion

5.1. Advantages and limitations of the two-stage calibration

The two-stage calibration procedure presented in this study was intended to balance the computational efficiency of a surrogate model in the first stage with the accuracy of the full CP model in the second stage. In addition, grain-average stresses, mimicking results of an HEDM experiment, were made available in the second stage to demonstrate the importance of including local data in the calibration. All one-stage and two-stage calibrations that included the grain-average stresses have less uncertainty in the posterior distributions, particularly for m and g_0 , than calibrations using the mean stresses only. Interestingly, in Section 4.3, the reduced grain stresses case showed clear bias in the posterior distributions for m and g_0 , but this bias was not present in the increased noise case. Therefore, the quantity of local calibration data may be more important than the precision of the data, although further study is needed on the influence of realistic noise on the local data. Another interesting result is that including local data significantly reduces uncertainty in the inverse rate sensitivity, m , even though the data is only available at a single global strain rate. The reduced uncertainty suggests that the individual grains are seeing different local effective strain rates. As a result, matching the grain-average stress data requires a more accurate value of m .

The computational cost for the calibration in Fig. 10b (one-stage calibration using the CP model with mean and grain-average stresses) is about twice the cost of the two-stage calibration. The number of SMC steps is also higher than for the second stage in the two-stage calibration, but only by about 22%. The reason for this disparity is that using the posteriors from the first stage regularizes the calibration via the prior. The regularization reduces the number of computationally-challenging samples in the first few SMC steps, such as samples with high g_0/g_1 or high m , in the second stage. As a result, in the first 72 hours, the one-stage calibration completed only 8 SMC steps while the second stage in the two-stage calibration completed 14 SMC steps. Thus, using the posteriors from the first stage as priors in the second stage can reduce computational cost two ways: reducing the required number of SMC steps and, in some cases, eliminating parameter combinations within the support of the original priors that result in longer CP simulations. On the other hand, the surrogate model training cost should also be considered for the two-stage calibration. The training simulations can be independently run in parallel across all available cores. As an example, assuming 1000 total simulations and an average of 30 minutes per simulation, 500 CPU hours would be added to the computational cost (which was about 2400 days for the two-stage calibration). With the same 644 cores as the two-step calibration, training would add only one hour of walltime.

The two-stage results in Fig. 7 and the results for a surrogate model using both mean and grain-average stresses in Fig. 10c highlight the benefits and pitfalls of using surrogate models. First, evaluating the surrogate incurs negligible computational cost compared to the full CP model in the SMC algorithm. Calibration with the surrogate model also helped to determine which parameters were likely to be more or less difficult to calibrate accurately. Here, results from the surrogate helped identify non-physical combinations of H and H_d and also indicated that m and g_0 would likely be easier to calibrate. The main tradeoff is bias in the posterior distributions due to error in the surrogate. For example, in the first stage of the two-stage calibration (Fig. 7a), the mode of the posterior distribution of H was biased toward values below the ground truth. The second mode at low values of H in Fig. 7c suggests that this bias may have propagated through to the final posteriors after the second stage. In other words, the amount of data available in the second stage may not have been sufficient to completely counteract the bias in the prior. The surrogate bias also becomes more significant with more degrees of freedom, as shown by the posteriors in Fig. 10c, where a surrogate was used for both the mean and grain-average stresses. In summary, including a calibration stage with the full CP model is crucial for counteracting any surrogate bias, but strong bias may still impact the final result of a two-stage calibration.

Instead of the surrogate, a less expensive CP model could be used in the first stage. The inexpensive model would need to have either the same material parameters or a subset of the material parameters of the full-field CP model. Homogenized models like those of Taylor (1934) and Sachs (1928) or the viscoplastic self-consistent model (Lebensohn and Tomé, 1993) are one option. Another option could be a full-field model with a significantly coarsened discretization. The inexpensive model may also be able to efficiently identify

non-physical or computationally challenging input parameter combinations, without needing potentially expensive training data from the full-field model like the surrogate used in this study. Nonetheless, problems due to bias of the inexpensive model still remain, due to the simplifying assumptions of the model as noted in the two-stage procedure of Depriester et al. (2023). The large number of possible inexpensive models invites the use of multi-fidelity methods, which are designed to eliminate bias from low-fidelity models and have been applied to uncertainty propagation in CP (Tran et al., 2023; Pribe et al., 2025). Recent work has investigated applying multi-fidelity Monte Carlo strategies to MCMC algorithms (Dodwell et al., 2019).

5.2. Algorithmic considerations for SMC

The embarrassingly parallelizable nature of SMC was crucial for completing any calibrations that used the full CP model in this study. Little SMC hyperparameter tuning was performed, so it is likely that improved sampling could be achieved. For example, one tunable hyperparameter is the number of MCMC proposals within each SMC step. The optimal value is the smallest number of proposals that achieves a mutation ratio close to 1.0, where the mutation ratio represents the proportion of particles that have moved to a new location in the parameter space during the SMC step. The use of five MCMC proposals here typically achieved mutation ratios between 0.6 and 0.9. One possible use of the surrogate model would be to run multiple calibrations in order to estimate the optimal number of MCMC steps from the mutation ratios, assuming that the number will be similar for SMC runs with the CP model.

The SMC algorithm also likely struggled to sample from the joint distributions of H and g_0/g_1 (Fig. 8) due to the correlation structure. These joint distributions are similar to so-called “banana-shaped distributions”, which are used as a test case for adaptive proposals in MCMC-based algorithms (Haario et al., 1999). The posterior distributions of parameters like H and g_0/g_1 could be sampled more efficiently by, for example, using estimates of the correlation between the parameters to guide the proposals for the MCMC steps (Sejdinovic et al., 2014; Schuster et al., 2017). Making derivatives available by incorporating autodifferentiation into the CP solver (Pundir and Kammer, 2025) could further improve the MCMC proposals and increase efficiency of the SMC algorithm.

5.3. Implications for calibration with real measurement data and more complex models

Two important considerations when setting up a CP model are choosing an appropriate constitutive model and identifying the required calibration data. The results of this study suggest that the portion of the stress-strain curve that is relevant to the intended model application should inform model selection. It is possible that 1% mean strain simply was not sufficiently far into the saturation part of the stress-strain curve to confidently calibrate the hardening parameters H and g_0/g_1 . If strains beyond 1% are not relevant to the intended application, this might be an indication that a different hardening model should be chosen. The strong correlation between H and g_0/g_1 (e.g., Fig. 8) also highlights the importance of having model

parameters that can be uniquely identified. Meanwhile, the significantly reduced uncertainty in m and g_0 when grain-average stresses are included in the calibration demonstrates the value of measuring local data.

Interestingly, Sedighiani et al. (2020) obtained similar results to the current study using a genetic algorithm-based calibration with synthetic global uniaxial stress data. The data was generated from one microstructure but at several different strain rates to study calibrations for several hardening laws. For a saturation-type hardening law, they obtained a unique parametrization for the initial CRSS and rate sensitivity but not for the hardening parameters, which were also found to be correlated with one another. The calibration data included strains out to 40%, which indicates that the correlation structure and identifiability challenges may persist even with data at higher strains, although Sedighiani et al. (2020) did not use any local data in their calibration.

Another interesting finding related to identifiability comes from the training data for the surrogate models. Two surrogate models were used in this study: one for the mean stresses only (used in the first stage of the two-stage calibration) and one for the mean and grain-average stresses (used in the comparisons in Section 4.4). Both surrogates were trained using the PCs of the corresponding training data sets, truncated such that the total explained variance was at least 99.9%. This resulted in four PCs for the mean stresses and six PCs for the mean and grain-average stresses. The explained variance for each PC is shown in Fig. 11. The explained variances are remarkably similar for both training datasets, even though the dimensionality of the second dataset is much larger due to including the grain-average stresses. Thus, the main benefit of the local data here may be simply increasing the amount of calibration data at different effective strain rates, rather than adding knowledge of the physics at smaller length scales. The grain-average stresses may be more heterogeneous in cases with stronger anisotropy, such as hexagonal close-packed metals or slip families having a clear distinction between self and latent hardening.

A relatively simple constitutive model was chosen for this study to enable interpretable results, but caution was still required in setting up the calibration problem. To avoid sampling non-physical input combinations in the surrogate training data and in the SMC algorithm, the derived parameter g_1/g_0 was used instead of the dynamic recovery coefficient in the calibration. Alternatively, joint priors encoding physical constraints could have been specified for g_0 , H , and H_d . The possibility of sampling physically unreasonable areas of the parameter space likely increases with the number of calibration parameters. This problem highlights the importance of using sensitivity analyses to determine which parameters are most important for predicting particular quantities of interest. Running inexpensive calibrations using synthetic data and a surrogate model, as in the first stage of the two-stage calibration in this study, can also be a helpful sanity check for determining the feasibility of the calibration problem and identifying challenging parameters. Thus, especially in more complicated models, it is valuable to have constitutive model parameters with a clear physical meaning.

An interesting approach to simultaneously address parameter uniqueness challenges and increase phys-

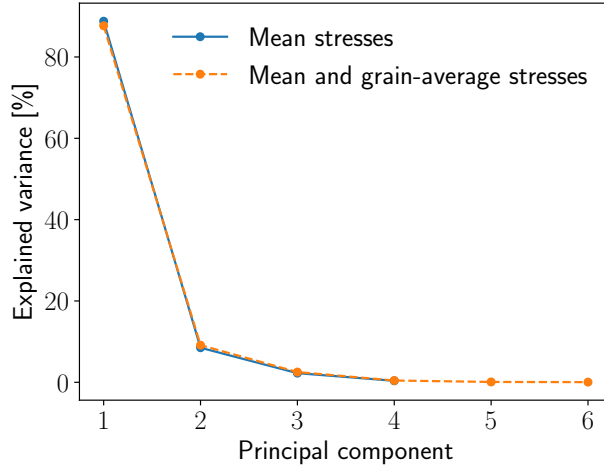


Figure 11: Explained variances, expressed as percentages, for the PCs of (a) the mean stress training data (used for the surrogate model in Section 4.1) and (b) the mean and grain-average stress training data (used for the surrogate model in Section 4.4).

ical meaning of the parameters has recently been developed by Castelluccio and co-workers (Ashraf and Castelluccio, 2021; Dindarlou and Castelluccio, 2022; Ashraf and Castelluccio, 2023; Dindarlou and Castelluccio, 2024). They proposed physics-based CP models whose forms and parametrizations are based on mesoscale dislocation mechanics. The parameters in turn have unique influences on specific measurable quantities, enabling sequential targeted measurements for identifying each parameter. An additional benefit of physics-based model forms is that model discrepancy can often be associated with missing physics in the model. Future work could consider a combination of this physics-based calibration for parts of a constitutive model and the statistical approach in the current study for behavior due to, for example, complex hardening mechanisms that requires a phenomenological description.

Finally, when calibrating with real data, model discrepancy related to the microstructural representation, boundary conditions, and CP model itself must be considered. Here, the original microstructure from Stinville et al. (2022) was simplified, primarily by merging twins, to obtain a microstructure more typical of HEDM experiments. The 32 grains that provided the local data in this study were similar to the 28 “relatively equiaxed and not highly twinned” grains chosen as challenge grains in the AFRL additive manufacturing modeling challenge for in-situ mechanical testing (Menasche et al., 2021). For a heavily twinned microstructure or one with columnar grains typical of some additive manufacturing processes, HEDM may not be the best option for obtaining local data. In addition to microstructural considerations, Hoc et al. (2003) showed that using inhomogeneous boundary conditions inferred from DIC for a region of interest in a polycrystal (rather than the global uniaxial tension boundary conditions) significantly improved local strain predictions. A related consideration for studies using HEDM data is the question of how to

represent the bulk material surrounding the microstructural region of interest. Here, a simple elastic and perfectly plastic material with yield strength below the microstructural region was used, primarily to break the periodic boundary conditions while still constraining the model. In reality, the buffer material properties would likely need to be tied to the microstructural region or estimated from the global stress-strain data. CP model form error can be addressed by adding a model discrepancy term to the likelihood (Eq. (5)) as in the Kennedy-O’Hagan approach for Bayesian inference (Kennedy and O’Hagan, 2001). The discrepancy term, especially when it is large, tends to exacerbate uniqueness challenges (Higdon et al., 2004); thus, strategies to distinguish between the effects of model parameter uncertainty and model discrepancy would need to be considered (Arendt et al., 2012; Brynjarsdóttir and O’Hagan, 2014).

6. Summary and conclusions

In this study, a two-stage probabilistic calibration approach was developed for CP models and demonstrated with synthetic measurement data. The approach balances computational cost with accuracy by using a surrogate model in the first stage and the full-field CP model in the second stage. Local data in the form of grain-average stresses was added in the second stage. Iterations on the two-stage approach explored robustness of the method to degradation in the local data and compared it with several one-stage calibrations. Analyzing the posterior distributions for the calibration parameters demonstrated the benefits of including local data and revealed causes of uncertainty and bias in the calibration. Overall, the results support the following conclusions:

- Including local data (grain-average stresses) in the calibration significantly reduces uncertainty in estimates of the initial CRSS and rate sensitivity. Uncertainty is also somewhat reduced for the hardening parameters H and H_d , but uniquely identifying these parameters is challenging with the available data.
- Correlations between parameters can make unique parameter identification from a calibration procedure difficult or impossible. This may be due to inherent correlations from the constitutive model form or the lack of necessary experimental data. Parameter identifiability should therefore be a consideration in selecting a constitutive law and designing the calibration experiments.
- SMC enables tractable Bayesian inference with a full-field CP model by using independent, parallel model evaluations to sample from the parameter posterior distributions.
- Using informed priors from calibration with a surrogate model (i.e., from stage one in the two-stage calibration) further reduces the computational expense by reducing the number of required SMC steps and eliminating non-physical or more expensive parameter combinations from the support of the

prior. On the other hand, bias from the surrogate model in the first stage can propagate through to the parameter posterior distributions in the second stage.

- The reduced uncertainty in the initial CRSS and rate sensitivity are robust to degradation of the local data (i.e., the “reduced grain stresses” and “increased noise” cases), but reducing the availability of the local data introduces bias to both parameters. This result suggests that experiments should focus on increasing the quantity rather than the precision of local data, although further detailed study is needed on this point.
- Using a surrogate model with both global and local data in the calibration produced posterior distributions with similar uncertainty but significantly more bias than the two-stage procedure. Surrogate models are thereby useful to identify the type and amount of data that should be used for calibration. However, the resulting calibration will likely be biased and may lead to poor predictive capability.

Declaration of competing interests

The authors declare that they have no known competing financial interests or personal relationships that could have appeared to influence the work reported in this paper.

Data availability

The Materialite code used for the crystal plasticity simulations is available at <https://github.com/nasa/materialite>. The SMCPy code used in the SMC calibration runs is available at <https://github.com/nasa/SMCPy>.

Acknowledgements

The authors gratefully acknowledge support from the Transformational Tools and Technologies Project in the NASA Aeronautics Research Mission Directorate. The authors also would like to thank Julia Truong, an intern at NASA Langley Research Center in 2025, for her contributions to the SMCPy code.

Appendix A. Fourier-Galerkin solution method

First, the strain, $\boldsymbol{\varepsilon}$, is expressed as

$$\boldsymbol{\varepsilon}(\mathbf{x}) = \mathbf{E} + \boldsymbol{\varepsilon}^*(\mathbf{x}) \quad \forall \mathbf{x} \in \Omega, \quad (\text{A.1})$$

where \mathbf{x} is a point in an Ω -periodic domain, \mathbf{E} is the mean strain in the domain, and $\boldsymbol{\varepsilon}^*$ is the fluctuation strain, representing the difference between the strain at a point and the mean strain. The strain field must be compatible, and the stress, $\boldsymbol{\sigma}$, which is a nonlinear function of the strain, must satisfy equilibrium:

$$\nabla \cdot \boldsymbol{\sigma}(\mathbf{x}) = \mathbf{0}, \quad \boldsymbol{\sigma}(\mathbf{x}) = \boldsymbol{\sigma}(\boldsymbol{\varepsilon}(\mathbf{x})). \quad (\text{A.2})$$

The weak form for this problem is

$$\int_{\Omega} \delta \boldsymbol{\varepsilon}^*(\mathbf{x}) : \boldsymbol{\sigma}(\mathbf{x}) d\mathbf{x} = 0, \quad (\text{A.3})$$

where $\delta \boldsymbol{\varepsilon}^*$ is a test strain. Due to periodicity of the strain field, there are no boundary terms in the weak form. Compatibility of the test strains is enforced using a projection operator, \mathbb{G} :

$$\delta \boldsymbol{\varepsilon}^*(\mathbf{x}) = (\mathbb{G} * \boldsymbol{\zeta})(\mathbf{x}), \quad (\text{A.4})$$

where $*$ represents convolution and $\boldsymbol{\zeta}$ is a second-order tensor field whose compatible part is $\delta \boldsymbol{\varepsilon}^*$. The operator \mathbb{G} maps second-order tensors to their compatible and symmetric part and has a closed-form expression in frequency space. See Appendix B for details on the construction of \mathbb{G} . \mathbb{G} is also self-adjoint, allowing the weak form to be written as

$$\int_{\Omega} \delta \boldsymbol{\zeta}(\mathbf{x}) : (\mathbb{G} * \boldsymbol{\sigma})(\mathbf{x}) d\mathbf{x} = 0. \quad (\text{A.5})$$

The domain is discretized on a regular grid of voxels, and the stress and strain fields are interpolated using trigonometric polynomial shape functions. This approach mirrors standard finite element methods, but the nodes and integration points are co-located at the centers of the voxels. Evaluating Eq. (A.5) using the trapezoidal rule with the interpolated fields and the convolution theorem leads to the discretized or nodal equilibrium equation (Zeman et al., 2017):

$$\mathcal{F}^{-1} \left[\hat{\mathbb{G}}(\boldsymbol{\xi}) \mathcal{F}[\boldsymbol{\sigma}(\mathbf{x})] \right] = \mathbf{0}, \quad (\text{A.6})$$

where $\mathcal{F}[\cdot]$ represents the Fourier transform, $\hat{\mathbb{G}}$ is the Fourier transform of \mathbb{G} , and $\boldsymbol{\xi}$ are the frequencies in Fourier space. To simplify notation on the left-hand side of Eq. (A.6), the mapping \mathcal{G} is defined as

$$\mathcal{G}[\cdot] := \mathcal{F}^{-1} \left[\hat{\mathbb{G}}(\boldsymbol{\xi}) \mathcal{F}[\cdot] \right]. \quad (\text{A.7})$$

This equation is evaluated at all of the nodes or voxel centers. For nonlinear problems, Eq. (A.6) is solved iteratively using the Newton-Raphson method. In iteration $i + 1$, the stress field is approximated as

$$\boldsymbol{\sigma}_{(i+1)} \approx \boldsymbol{\sigma}_{(i)} + \mathbb{C}_{(i)} \Delta \boldsymbol{\varepsilon}_{(i+1)}^* \quad (\text{A.8})$$

where $\mathbb{C}_{(i)}$ is the consistent tangent operator from iteration i , and the dependence on \mathbf{x} has been dropped to simplify notation. Inserting the stress approximation into Eq. (A.6) gives

$$\mathcal{G} \left[\mathbb{C}_{(i)} \Delta \boldsymbol{\varepsilon}_{(i+1)}^* \right] = -\mathcal{G}[\boldsymbol{\sigma}_{(i)}] \quad (\text{A.9})$$

Using the fast Fourier transform (FFT), the action of \mathcal{G} can be expressed using a sequence of matrix operations. As a result, Eq. (A.9) can be expressed as a linear system of equations, $\mathcal{A}\Delta\boldsymbol{\varepsilon}_{(i+1)}^* = \mathbf{b}$, where \mathcal{A} is the system matrix and \mathbf{b} is the right-hand side of Eq. (A.9). The system is solved for $\Delta\boldsymbol{\varepsilon}_{(i+1)}^*$ in each iteration using conjugate gradients, which ensures that a compatible strain field is returned in each iteration (Mishra et al., 2016). The updated stress and consistent tangent are then obtained from the constitutive model. Unlike FFT-based methods that rely on a reference medium, the consistent tangent is identical to the one in a typical finite element material subroutine.

Here, the consistent tangent is approximated by differentiating Eqs. (1) and (2):

$$\mathbb{C} = \frac{\partial \boldsymbol{\sigma}}{\partial \boldsymbol{\varepsilon}} = \left(\mathbb{I}_{\text{sym}} + \mathbb{D} \frac{\partial \dot{\boldsymbol{\varepsilon}}_p}{\partial \boldsymbol{\sigma}} \right)^{-1} \mathbb{D}, \quad (\text{A.10})$$

where \mathbb{I}_{sym} is the fourth-order symmetric identity tensor, and the unknown derivative is given by

$$\frac{\partial \dot{\boldsymbol{\varepsilon}}_p}{\partial \boldsymbol{\sigma}} \approx m \dot{\gamma}_0 \sum_{s=1}^{N_s} \frac{\mathbf{m}_s \otimes \mathbf{m}_s}{g_s} \left(\frac{\mathbf{m}_s : \boldsymbol{\sigma}}{g_s} \right)^{m-1}. \quad (\text{A.11})$$

Note that the contribution from the hardening law has been neglected in Eq. (A.11).

Appendix B. Projection tensor and boundary conditions

For the nonzero, non-Nyquist frequencies, the projection tensor is given in index notation by

$$\hat{\mathbb{G}}(\boldsymbol{\xi}) = \hat{G}_{ijkl}(\boldsymbol{\xi}) = \frac{1}{2} \frac{\xi_i \delta_{jk} \xi_l + \xi_i \delta_{jl} \xi_k + \xi_j \delta_{ik} \xi_l + \xi_j \delta_{il} \xi_k}{\|\boldsymbol{\xi}\|^2} - \frac{\xi_i \xi_j \xi_k \xi_l}{\|\boldsymbol{\xi}\|^4}. \quad (\text{B.1})$$

Note that $\boldsymbol{\xi}$ represents scaled frequencies, with $\xi_i = k_i/L_i$, where k_i is the raw frequencies and L_i is the number of points in the domain in the i^{th} direction. Following de Geus et al. (2017), the projection tensor is set to zero at the Nyquist frequencies since the grid used in this study has an even number of points. Following Lucarini and Segurado (2019), the components of the projection tensor at the zero frequency are set based on the boundary conditions:

- If component ij is under strain control, then $\hat{G}_{ijkl}(\mathbf{0})$ is set to zero: $\hat{G}_{ijkl}(\mathbf{0}) = 0_{ijkl}$.
- If component ij is under stress control, then $\hat{G}_{ijkl}(\mathbf{0})$ is set to the corresponding component of the symmetric identity tensor: $\hat{G}_{ijkl}(\mathbf{0}) = \frac{1}{2} (\delta_{ik} \delta_{jl} + \delta_{il} \delta_{jk})$.

For the boundary conditions in this study (uniaxial strain in the x direction, with all other components stress free), the 11 component is under strain control, and the remaining five components are under stress

control. Thus, the full piecewise definition of the projection tensor is

$$\hat{G}_{ijkl}(\boldsymbol{\xi}) = \begin{cases} 0_{ijkl}, & \text{Nyquist frequencies} \\ 0_{ijkl}, & \boldsymbol{\xi} = \mathbf{0} \text{ and } ij = 11 \text{ (strain control)} \\ \frac{1}{2} (\delta_{ik}\delta_{jl} + \delta_{il}\delta_{jk}), & \boldsymbol{\xi} = \mathbf{0} \text{ and } ij \neq 11 \text{ (stress control)} \\ \frac{1}{2} \frac{\xi_i \delta_{jk} \xi_l + \xi_i \delta_{jl} \xi_k + \xi_j \delta_{ik} \xi_l + \xi_j \delta_{il} \xi_k}{\|\boldsymbol{\xi}\|^2} - \frac{\xi_i \xi_j \xi_k \xi_l}{\|\boldsymbol{\xi}\|^4}, & \text{otherwise} \end{cases} \quad (\text{B.2})$$

Appendix C. Principal component analysis for the training data

To train the neural network surrogate model in Section 4.1, PCA was conducted on the mean stresses from the 900 training samples. Specifically, this involves determining the PCs of the matrix containing the 13 mean stress values from each sample:

$$\begin{array}{c} \text{Mean stresses} \\ \left[\begin{array}{cccc} \Sigma_{11}^{(1,1)} & \Sigma_{11}^{(1,2)} & \dots & \Sigma_{11}^{(1,13)} \\ \Sigma_{11}^{(2,1)} & \Sigma_{11}^{(2,2)} & \dots & \Sigma_{11}^{(2,13)} \\ \vdots & \vdots & \ddots & \vdots \\ \Sigma_{11}^{(900,1)} & \Sigma_{11}^{(900,2)} & \dots & \Sigma_{11}^{(900,13)} \end{array} \right] \end{array} \quad (\text{C.1})$$

where each row represents a sample and each column represents a feature (one of the stresses from the mean stress-strain curve) such that $\Sigma_{11}^{(i,j)}$ represents the j^{th} mean stress for the i^{th} sample. The PCs of this matrix represent the directions of maximum variance in the 13-dimensional feature space. Two properties of the PCs are useful here:

1. Each PC explains a percentage of the variance in the dataset. The first PC explains the most variance, while the 13th PC explains the least. Choosing the first $M < 13$ PCs reduces the dimensionality of the feature space, where M can be chosen such that a desired percentage of the variance is explained (here, 99.9% of the variance, resulting in $M = 4$).
2. The PCs are independent, while the original features are highly correlated as inferred from Fig. 6.

More importantly, the independence of the PCs simplified training of the neural network and resulted in more physically realistic stress-strain curve predictions.

For the surrogate model in Section 4.4 trained on the mean *and* grain-average stresses from the 900 training samples, the data matrix becomes

$$\left[\begin{array}{cccccccccc} \Sigma_{11}^{(1,1)} & \dots & \Sigma_{11}^{(1,13)} & \sigma_{11,1}^{(1,1)} & \sigma_{11,1}^{(1,2)} & \dots & \sigma_{11,1}^{(1,13)} & \sigma_{11,2}^{(1,1)} & \dots & \sigma_{11,32}^{(1,13)} \\ \Sigma_{11}^{(2,1)} & \dots & \Sigma_{11}^{(2,13)} & \sigma_{11,1}^{(2,1)} & \sigma_{11,1}^{(2,2)} & \dots & \sigma_{11,1}^{(2,13)} & \sigma_{11,2}^{(2,1)} & \dots & \sigma_{11,32}^{(2,13)} \\ \vdots & \ddots & \vdots & \vdots & \vdots & \ddots & \vdots & \vdots & \ddots & \vdots \\ \Sigma_{11}^{(900,1)} & \dots & \Sigma_{11}^{(900,13)} & \sigma_{11,1}^{(900,1)} & \sigma_{11,1}^{(900,2)} & \dots & \sigma_{11,1}^{(900,13)} & \sigma_{11,2}^{(900,1)} & \dots & \sigma_{11,32}^{(900,13)} \end{array} \right] \quad (\text{C.2})$$

Table D.1: Statistics for the posterior distribution of m .

Calibration	MAP	Median	Mean	St. dev.	95% CI	95% CI length
First stage of two-stage calibration (Fig. 7a)	10.02	10.13	10.25	1.35	[7.96, 13.23]	5.27
End of two-stage calibration (Fig. 7b)	10.05	10.02	10.00	0.126	[9.77, 10.25]	0.482
Reduced grain stresses (Fig. 9b)	9.72	9.74	9.74	0.150	[9.46, 10.02]	0.563
Increased noise (Fig. 9c)	9.87	9.96	9.96	0.194	[9.60, 10.31]	0.708
One-stage CP model with mean stresses only (Fig. 10a)	9.52	9.93	9.98	0.861	[8.49, 11.81]	3.32
One-stage CP model with mean and grain-average stresses (Fig. 10b)	10.01	10.01	10.01	0.113	[9.80, 10.23]	0.435
One-stage surrogate with mean and grain-average stresses (Fig. 10c)	10.49	10.44	10.44	0.127	[10.20, 10.70]	0.815

where $\sigma_{11,m}^{(i,j)}$ represents the j^{th} grain-average stress from the m^{th} grain for the i^{th} sample. Now, each sample has 429 total features across the mean and grain-average stresses. Due to the increased dimensionality of the training data, the dimensionality reduction from principal component analysis becomes more powerful, in addition to the benefits of having independent features.

Appendix D. Summary statistics for the marginal posterior distributions

The tables in this appendix show six summary statistics for the marginal posterior distributions: maximum a posteriori (MAP) estimate, median, mean, standard deviation, 95% credible interval (CI) centered on the median, and the length of the 95% CI. The MAP estimates come from a KDE fit to the joint posterior in each case. The KDE fit may be less reliable for some of the more complex distributions, particularly H and g_0/g_1 . Larger differences between the MAP, median, and mean for these two parameters indicate reduced normality relative to the posterior distributions for m , g_0 , and σ_{noise} , which is also seen visually in the histograms in Section 4.

Table D.2: Statistics for the posterior distribution of g_0 . All numbers have units of MPa.

Calibration	MAP	Median	Mean	St. dev.	95% CI	95% CI length
First stage of two-stage calibration (Fig. 7a)	394.3	394.2	394.5	5.76	[384.0, 407.0]	23.0
End of two-stage calibration (Fig. 7b)	399.7	400.1	400.1	0.67	[398.7, 401.3]	2.63
Reduced grain stresses (Fig. 9b)	401.3	401.4	401.4	0.73	[400.0, 402.8]	2.81
Increased noise (Fig. 9c)	400.9	400.4	400.4	0.94	[398.7, 402.2]	3.49
One-stage CP model with mean stresses only (Fig. 10a)	398.2	395.8	395.9	4.08	[388.6, 404.2]	15.7
One-stage CP model with mean and grain-average stresses (Fig. 10b)	400.1	400.1	400.1	0.64	[398.8, 401.3]	2.56
One-stage surrogate with mean and grain-average stresses (Fig. 10c)	400.2	400.0	399.8	1.72	[395.7, 402.4]	6.74

Table D.3: Statistics for the posterior distribution of g_0 . All numbers have units of MPa.

Calibration	MAP	Median	Mean	St. dev.	95% CI	95% CI length
First stage of two-stage calibration (Fig. 7a)	9463	9937	12065	8376	[1520, 28572]	27052
End of two-stage calibration (Fig. 7b)	12311	7743	8155	434.6	[2155, 16524]	14369
Reduced grain stresses (Fig. 9b)	6264	5864	6825	3472	[2873, 16239]	13366
Increased noise (Fig. 9c)	4328	4116	5328	2966	[2430, 12881]	10452
One-stage CP model with mean stresses only (Fig. 10a)	9306	10698	12189	7105	[2825, 27713]	24889
One-stage CP model with mean and grain-average stresses (Fig. 10b)	8285	8306	9020	3792	[3662, 17347]	13685
One-stage surrogate with mean and grain-average stresses (Fig. 10c)	1779	2101	2782	2426	[1044, 9255]	8211

Table D.4: Statistics for the posterior distribution of g_0/g_1 .

Calibration	MAP	Median	Mean	St. dev.	95% CI	95% CI length
First stage of two-stage calibration (Fig. 7a)	0.687	0.718	0.606	0.246	[0.065, 0.873]	0.808
End of two-stage calibration (Fig. 7b)	0.831	0.752	0.671	0.205	[0.193, 0.861]	0.668
Reduced grain stresses (Fig. 9b)	0.713	0.707	0.692	0.121	[0.435, 0.879]	0.443
Increased noise (Fig. 9c)	0.585	0.572	0.574	0.170	[0.272, 0.838]	0.566
One-stage CP model with mean stresses only (Fig. 10a)	0.718	0.737	0.685	0.177	[0.200, 0.887]	0.687
One-stage CP model with mean and grain-average stresses (Fig. 10b)	0.763	0.769	0.749	0.092	[0.531, 0.870]	0.339
One-stage surrogate with mean and grain-average stresses (Fig. 10c)	0.333	0.378	0.415	0.145	[0.241, 0.806]	0.565

Table D.5: Statistics for the posterior distribution of σ_{noise} . All numbers have units of MPa.

Calibration	MAP	Median	Mean	St. dev.	95% CI	95% CI length
First stage of two-stage calibration (Fig. 7a)	6.24	7.32	7.72	2.12	[4.82, 13.0]	8.18
End of two-stage calibration (Fig. 7b)	5.22	5.24	5.23	0.151	[4.91, 5.52]	0.618
Reduced grain stresses (Fig. 9b)	5.16	5.18	5.20	0.251	[4.74, 5.72]	0.984
Increased noise (Fig. 9c)	6.92	6.85	6.97	1.29	[4.90, 9.78]	4.88
One-stage CP model with mean stresses only (Fig. 10a)	5.69	6.61	6.88	1.72	[4.42, 11.0]	6.55
One-stage CP model with mean and grain-average stresses (Fig. 10b)	5.34	5.24	5.24	0.163	[4.92, 5.55]	0.622
One-stage surrogate with mean and grain-average stresses (Fig. 10c)	5.98	5.98	5.98	0.208	[5.59, 6.41]	0.815

References

- Anand, L., Kothari, M., 1996. A computational procedure for rate-independent crystal plasticity. *Journal of the Mechanics and Physics of Solids* 44, 525–558. URL: <https://linkinghub.elsevier.com/retrieve/pii/0022509696000014>, doi:10.1016/0022-5096(96)00001-4.
- Arendt, P.D., Apley, D.W., Chen, W., Lamb, D., Gorsich, D., 2012. Improving identifiability in model calibration using multiple responses. *J Mech Des* 134, 100909. doi:10.1115/1.4007573.
- Ashraf, F., Castelluccio, G.M., 2021. A robust approach to parameterize dislocation glide energy barriers in FCC metals and alloys. *J Mater Sci* 56, 16491–16509. doi:10.1007/s10853-021-06376-1.
- Ashraf, F., Castelluccio, G.M., 2023. History and temperature dependent cyclic crystal plasticity model with material-invariant parameters. *Int J Plast* 161, 103494. doi:10.1016/j.ijplas.2022.103494.
- Bandyopadhyay, R., Prithivirajan, V., Sangid, M.D., 2019. Uncertainty quantification in the mechanical response of crystal plasticity simulations. *JOM* 71, 2612–2624. doi:10.1007/s11837-019-03551-3.
- Bishop, J., Hill, R., 1951. A theoretical derivation of the plastic properties of a polycrystalline face-centered metal. *Philos Mag* 42, 1298–1307. doi:10.1080/14786444108561385.
- Brynjarsdóttir, J., O’Hagan, A., 2014. Learning about physical parameters: the importance of model discrepancy. *Inverse Problems* 30, 114007. doi:10.1088/0266-5611/30/11/114007.
- Cheng, J., Hu, X., Lach, T., Chen, X.F., 2024. A macro-micro approach for identifying crystal plasticity parameters for necking and failure in nickel-based alloy haynes 282. *Int J Plast* 178, 103997. doi:10.1016/j.ijplas.2024.103997.
- Del Moral, P., Doucet, A., Jasra, A., 2006. Sequential monte carlo samplers. *J R Stat Soc Ser B Stat Methodol* 68, 411–436. doi:10.1111/j.1467-9868.2006.00553.x.
- Del Moral, P., Doucet, A., Jasra, A., 2012. On adaptive resampling strategies for sequential Monte Carlo methods. *Bernoulli* 18. doi:10.3150/10-BEJ335.
- Depriester, D., Goulmy, J.P., Barrallier, L., 2023. Crystal plasticity simulations of in situ tensile tests: A two-step inverse method for identification of CP parameters, and assessment of CPFEM capabilities. *Int J Plast* 168, 103695. doi:10.1016/j.ijplas.2023.103695.
- Dindarlou, S., Castelluccio, G.M., 2022. Substructure-sensitive crystal plasticity with material-invariant parameters. *Int J Plast* 155, 103306. doi:10.1016/j.ijplas.2022.103306.
- Dindarlou, S., Castelluccio, G.M., 2024. Optimization of crystal plasticity parameters with proxy materials data for alloy single crystals. *Int J Plast* 174, 103894. doi:10.1016/j.ijplas.2024.103894.
- Dodwell, T.J., Ketelsen, C., Scheichl, R., Teckentrup, A.L., 2019. Multilevel Markov Chain Monte Carlo. *SIAM Review* 61, 509–545. doi:10.1137/19M126966X. eprint: <https://doi.org/10.1137/19M126966X>.
- Fernandez-Zelaia, P., Lee, Y., Dryepondt, S., Kirka, M.M., 2022. Creep anisotropy modeling and uncertainty quantification of an additively manufactured Ni-based superalloy. *Int J Plast* 151, 103177. doi:10.1016/j.ijplas.2021.103177.
- de Geus, T.W.J., Vondřejc, J., Zeman, J., Peerlings, R.H.J., Geers, M.G.D., 2017. Finite strain FFT-based non-linear solvers made simple. *Comput Methods Appl Mech Eng* 318, 412–430. doi:10.1016/j.cma.2016.12.032.
- Ghorbanpour, S., Zecevic, M., Kumar, A., Jahedi, M., Bicknell, J., Jorgensen, L., Beyerlein, I.J., Knezevic, M., 2017. A crystal plasticity model incorporating the effects of precipitates in superalloys: Application to tensile, compressive, and cyclic deformation of Inconel 718. *Int J Plast* 99, 162–185. doi:10.1016/j.ijplas.2017.09.006.
- Haario, H., Saksman, E., Tamminen, J., 1999. Adaptive proposal distribution for random walk Metropolis algorithm. *Comput Stat* 14, 375–395. doi:10.1007/s001800050022.
- Herrera-Solaz, V., LLorca, J., Dogan, E., Karaman, I., Segurado, J., 2014. An inverse optimization strategy to determine single crystal mechanical behavior from polycrystal tests: Application to AZ31 Mg alloy. *Int J Plast* 57, 1–15. doi:10.1016/j.ijplas.2014.02.001.

- Higdon, D., Kennedy, M., Cavendish, J.C., Cafeo, J.A., Ryne, R.D., 2004. Combining field data and computer simulations for calibration and prediction. *SIAM J Sci Comput* 26, 448–466. doi:10.1137/S1064827503426693.
- Hoc, T., Crépin, J., Gélébart, L., Zaoui, A., 2003. A procedure for identifying the plastic behavior of single crystals from the local response of polycrystals. *Acta Mater* 51, 5477–5488. doi:10.1016/S1359-6454(03)00413-0.
- Hochhalter, J., Bomarito, G., Yeratapally, S., Leser, P., Ruggles, T., Warner, J., Leser, W., 2020. Non-deterministic calibration of crystal plasticity model parameters, in: Ghosh, S., Woodward, C., Przybyla, C. (Eds.), *Integrated Computational Materials Engineering (ICME)*. Springer International Publishing, Cham, pp. 165–198.
- Kapoor, K., Ravi, P., Noraas, R., Park, J.S., Venkatesh, V., Sangid, M.D., 2021. Modeling Ti–6Al–4V using crystal plasticity, calibrated with multi-scale experiments, to understand the effect of the orientation and morphology of the α and β phases on time dependent cyclic loading. *J Mech Phys Solids* 146, 104192. doi:10.1016/j.jmps.2020.104192.
- Kennedy, M.C., O’Hagan, A., 2001. Bayesian calibration of computer models. *J R Stat Soc Ser B Stat Methodol* 63, 425–464. doi:10.1111/1467-9868.00294.
- Kuhn, J., Spitz, J., Sonnweber-Ribic, P., Schneider, M., Böhlke, T., 2022. Identifying material parameters in crystal plasticity by Bayesian optimization. *Optim Eng* 23, 1489–1523. doi:10.1007/s11081-021-09663-7.
- Lebensohn, R.A., Rollett, A.D., 2020. Spectral methods for full-field micromechanical modelling of polycrystalline materials. *Comput Mater Sci* 173, 109336. doi:10.1016/j.commatsci.2019.109336.
- Lebensohn, R.A., Tomé, C.N., 1993. A self-consistent anisotropic approach for the simulation of plastic deformation and texture development of polycrystals: Application to zirconium alloys. *Acta Metall Mater* 41, 2611–2624. doi:10.1016/0956-7151(93)90130-K.
- Leser, P.E., Hochhalter, J.D., Warner, J.E., Bomarito, G.F., Leser, W.P., Yuan, F.G., 2018. Sequential Monte Carlo: Enabling real-time and high-fidelity prognostics. *Annual Conference of the PHM Society* 10. doi:10.36001/phmconf.2018.v10i1.564.
- Liu, W., Lian, J., Aravas, N., Münstermann, S., 2020. A strategy for synthetic microstructure generation and crystal plasticity parameter calibration of fine-grain-structured dual-phase steel. *Int J Plast* 126, 102614. doi:10.1016/j.ijplas.2019.10.002.
- Lodh, A., Keller, C., Castelluccio, G.M., 2023. Fabrication and mechanical testing of mesoscale specimens. *JOM* 75, 2473–2479. doi:10.1007/s11837-023-05857-9.
- Lucarini, S., Segurado, J., 2019. An algorithm for stress and mixed control in Galerkin-based FFT homogenization. *Int J Numer Meth Engr* 119, 797–805. doi:10.1002/nme.6069.
- Mackey, B.T., Bandyopadhyay, R., Gustafson, S.E., Sangid, M.D., 2023. Grain interactions under thermo-mechanical loads investigated with coupled crystal plasticity simulations and high-energy X-ray diffraction microscopy. *Acta Mater* 257, 119166. doi:10.1016/j.actamat.2023.119166.
- Menasche, D.B., Musinski, W.D., Obstalecki, M., Shah, M.N., Donegan, S.P., Bernier, J.V., Kenesei, P., Park, J.S., Shade, P.A., 2021. AFRL Additive Manufacturing Modeling Series: Challenge 4, in situ mechanical test of an IN625 sample with concurrent high-energy diffraction microscopy characterization. *Integr Mater Manuf Innov* 10, 338–347. doi:10.1007/s40192-021-00218-3.
- Menasche, D.B., Shade, P.A., Kenesei, P., Park, J.S., Musinski, W.D., 2023. Four-dimensional microstructurally small fatigue crack growth in cyclically loaded nickel superalloy specimen. *Int J Fatigue* 177, 107920. doi:10.1016/j.ijfatigue.2023.107920.
- Mishra, N., Vondřejc, J., Zeman, J., 2016. A comparative study on low-memory iterative solvers for FFT-based homogenization of periodic media. *J Comput Phys* 321, 151–168. doi:10.1016/j.jcp.2016.05.041.
- Moulinec, H., Suquet, P., 1998. A numerical method for computing the overall response of nonlinear composites with complex microstructure. *Comput Methods Appl Mech Eng* 157, 69–94. doi:10.1016/S0045-7825(97)00218-1.
- Nguyen, T., Francom, D.C., Luscher, D.J., Wilkerson, J.W., 2021. Bayesian calibration of a physics-based crystal plasticity and damage model. *J Mech Phys Solids* 149, 104284. doi:10.1016/j.jmps.2020.104284.

- Obstalecki, M., Wong, S.L., Dawson, P.R., Miller, M.P., 2014. Quantitative analysis of crystal scale deformation heterogeneity during cyclic plasticity using high-energy X-ray diffraction and finite-element simulation. *Acta Mater* 75, 259–272. doi:10.1016/j.actamat.2014.04.059.
- Park, T., Hector, L.G., Hu, X., Abu-Farha, F., Fellingner, M.R., Kim, H., Esmailpour, R., Pourboghrat, F., 2019. Crystal plasticity modeling of 3rd generation multi-phase AHSS with martensitic transformation. *Int J Plast* 120, 1–46. doi:10.1016/j.ijplas.2019.03.010.
- Pedregosa, F., Varoquaux, G., Gramfort, A., Michel, V., Thirion, B., Grisel, O., Blondel, M., Prettenhofer, P., Weiss, R., Dubourg, V., Vanderplas, J., Passos, A., Cournapeau, D., Brucher, M., Perrot, M., Duchesnay, E., 2011. Scikit-learn: Machine learning in Python. *Journal of Machine Learning Research* 12, 2825–2830.
- Peirce, D., Asaro, R., Needleman, A., 1983. Material rate dependence and localized deformation in crystalline solids. *Acta Metallurgica* 31, 1951–1976. URL: <https://linkinghub.elsevier.com/retrieve/pii/0001616083900147>, doi:10.1016/0001-6160(83)90014-7.
- Pokharel, R., Lind, J., Kanjarla, A.K., Lebensohn, R.A., Li, S.F., Kenesei, P., Suter, R.M., Rollett, A.D., 2014. Polycrystal plasticity: Comparison between grain-scale observations of deformation and simulations. *Annu Rev Condens Matter Phys* 5, 317–346. doi:10.1146/annurev-conmatphys-031113-133846.
- Pribe, J.D., Leser, P.E., Yeratapally, S.R., Glaessgen, E.H., 2025. Multi-model Monte Carlo estimation for crystal plasticity structure–property simulations of additively manufactured metals. *Comput Mater Sci* 247, 113481. doi:10.1016/j.commatsci.2024.113481.
- Prithivirajan, V., Ravi, P., Naragani, D., Sangid, M.D., 2021. Direct comparison of microstructure-sensitive fatigue crack initiation via crystal plasticity simulations and in situ high-energy X-ray experiments. *Mater Des* 197, 109216. doi:10.1016/j.matdes.2020.109216.
- Pundir, M., Kammer, D.S., 2025. Simplifying FFT-based methods for solid mechanics with automatic differentiation. *Comput Methods Appl Mech Eng* 435, 117572. doi:10.1016/j.cma.2024.117572.
- Roters, F., Eisenlohr, P., Hantcherli, L., Tjahjanto, D., Bieler, T., Raabe, D., 2010. Overview of constitutive laws, kinematics, homogenization and multiscale methods in crystal plasticity finite-element modeling: Theory, experiments, applications. *Acta Mater* 58, 1152–1211. doi:10.1016/j.actamat.2009.10.058.
- Rovinelli, A., Guilhem, Y., Proudhon, H., Lebensohn, R.A., Ludwig, W., Sangid, M.D., 2017. Assessing reliability of fatigue indicator parameters for small crack growth via a probabilistic framework. *Modelling Simul Mater Sci Eng* 25, 045010. doi:10.1088/1361-651X/aa6c45.
- Sachs, G., 1928. Zur ableitung einer fließbedingung. *Z Ver Dtsch Ing* 72, 734–736.
- Sangid, M., Yeratapally, S.R., Rovinelli, A., 2014. Validation of microstructure-based materials modeling, in: 55th AIAA/ASME/ASCE/AHS/ASC Structures, Structural Dynamics, and Materials Conference, American Institute of Aeronautics and Astronautics, National Harbor, Maryland. doi:10.2514/6.2014-0462.
- Sangid, M.D., 2020. Coupling in situ experiments and modeling – Opportunities for data fusion, machine learning, and discovery of emergent behavior. *Curr Opin Solid State Mater Sci* 24, 100797. doi:10.1016/j.cossms.2019.100797.
- Schuster, I., Strathmann, H., Paige, B., Sejdinovic, D., 2017. Kernel sequential Monte Carlo, in: *Joint European Conference on Machine Learning and Knowledge Discovery in Databases*, Springer. pp. 390–409.
- Sedighiani, K., Diehl, M., Traka, K., Roters, F., Sietsma, J., Raabe, D., 2020. An efficient and robust approach to determine material parameters of crystal plasticity constitutive laws from macro-scale stress–strain curves. *Int J Plast* 134, 102779. doi:10.1016/j.ijplas.2020.102779.
- Sejdinovic, D., Strathmann, H., Garcia, M.L., Andrieu, C., Gretton, A., 2014. Kernel adaptive Metropolis-Hastings, in: *International Conference on Machine Learning*, PMLR. pp. 1665–1673.
- Shade, P.A., Musinski, W.D., Obstalecki, M., Pagan, D.C., Beaudoin, A.J., Bernier, J.V., Turner, T.J., 2019. Exploring new

- links between crystal plasticity models and high-energy X-ray diffraction microscopy. *Curr Opin Solid State Mater Sci* 23, 100763. doi:10.1016/j.cossms.2019.07.002.
- Shimanek, J.D., Liu, Z.K., Beese, A.M., 2024. Effects of misorientation on single crystal plasticity by finite element methods. *Comput Mater Sci* 237, 112879. doi:10.1016/j.commatsci.2024.112879.
- Shimanek, J.D., Liu, Z.K., Beese, A.M., 2025. Simultaneous optimization of crystal plasticity hardening parameters. *JOM* 77, 324–335. doi:10.1007/s11837-024-06935-2.
- Stinville, J.C., Hestroffer, J.M., Charpagne, M.A., Polonsky, A.T., Echlin, M.P., Torbet, C.J., Valle, V., Nygren, K.E., Miller, M.P., Klaas, O., Loghin, A., Beyerlein, I.J., Pollock, T.M., 2022. Multi-modal dataset of a polycrystalline metallic material: 3D microstructure and deformation fields. *Sci Data* 9, 460. doi:10.1038/s41597-022-01525-w.
- Taylor, G.I., 1934. The mechanism of plastic deformation of crystals. Part I.—Theoretical. *Proc R Soc A* 145, 362–387. doi:10.1098/rspa.1934.0106. eprint: <https://royalsocietypublishing.org/doi/pdf/10.1098/rspa.1934.0106>.
- Tran, A., Lim, H., 2023. An asynchronous parallel high-throughput model calibration framework for crystal plasticity finite element constitutive models. *Comput Mech* 72, 485–498. doi:10.1007/s00466-023-02308-9.
- Tran, A., Robbe, P., Rodgers, T., Lim, H., 2023. Multi-fidelity uncertainty quantification for homogenization problems in structure-property relationships from crystal plasticity finite elements. *JOM* doi:10.1007/s11837-023-06182-x.
- Veasna, K., Feng, Z., Zhang, Q., Knezevic, M., 2023. Machine learning-based multi-objective optimization for efficient identification of crystal plasticity model parameters. *Comput Methods Appl Mech Eng* 403, 115740. doi:10.1016/j.cma.2022.115740.
- Weber, G., Pinz, M., Ghosh, S., 2022. Machine learning-enabled self-consistent parametrically-upscaled crystal plasticity model for Ni-based superalloys. *Comput Methods Appl Mech Eng* 402, 115384. doi:10.1016/j.cma.2022.115384.
- Whelan, G., McDowell, D.L., 2019. Uncertainty quantification in ICME workflows for fatigue critical computational modeling. *Eng Fract Mech* 220, 106673. doi:10.1016/j.engfracmech.2019.106673.
- Yeratapally, S.R., Cerrone, A.R., Glaessgen, E.H., 2021. Discrepancy between crystal plasticity simulations and far-field high-energy X-ray diffraction microscopy measurements. *Integr Mater Manuf Innov* 10, 196–217. doi:10.1007/s40192-021-00216-5.
- Zeman, J., de Geus, T.W.J., Vondřejc, J., Peerlings, R.H.J., Geers, M.G.D., 2017. A finite element perspective on nonlinear FFT-based micromechanical simulations. *Int J Numer Meth Engr* 111, 903–926. doi:10.1002/nme.5481.
- Zhang, T., Jiang, J., Britton, B., Shollock, B., Dunne, F., 2016. Crack nucleation using combined crystal plasticity modelling, high-resolution digital image correlation and high-resolution electron backscatter diffraction in a superalloy containing non-metallic inclusions under fatigue. *Proc R Soc A* 472, 20150792. doi:10.1098/rspa.2015.0792.